

Filament turnover is essential for continuous long range contractile flow in a model actomyosin cortex.

William M McFadden<sup>1</sup>, Patrick M McCall<sup>2</sup>, Edwin M Munro<sup>3,\*</sup>

**1 Biophysical Sciences Program, University of Chicago, Chicago, IL, USA**

**2 Department of Physics, University of Chicago, Chicago, IL, USA**

**3 Department of Molecular Genetics and Cell Biology, University of Chicago, Chicago, IL, USA**

\* [emunro@uchicago.edu](mailto:emunro@uchicago.edu)

## Abstract

Actomyosin-based cortical flow is a fundamental engine for cellular morphogenesis. Cortical flows are generated by cross-linked networks of actin filaments and myosin motors, in which active stress produced by motor activity is opposed by passive resistance to network deformation. Continuous flow requires local remodeling through crosslink unbinding and and/or filament disassembly. But how local remodeling tunes stress production and dissipation, and how this in turn shapes long range flow, remains poorly understood. Here, we introduce a computational model for a cross-linked networks with active motors based on minimal requirements for production and dissipation of contractile stress, namely asymmetric filament compliance, spatial heterogeneity of motor activity, reversible cross-links and filament turnover. We characterize how the production and dissipation of network stress depend, individually, on cross-link dynamics and filament turnover, and how these dependencies combine to determine overall rates of cortical flow. Our analysis predicts that filament turnover is required to maintain active stress against external resistance and steady state flow in response to external stress. Steady state stress increases with filament lifetime up to a characteristic time  $\tau_m$ , then decreases with lifetime above  $\tau_m$ . Effective viscosity

increases with filament lifetime up to a characteristic time  $\tau_c$ , and then becomes independent of filament lifetime and sharply dependent on crosslink dynamics. These individual dependencies of active stress and effective viscosity define multiple regimes of steady state flow. In particular our model predicts the existence of a regime, when filament lifetimes are shorter than both  $\tau_c$  and  $\tau_m$ , in which dependencies of effective viscosity and steady state stress cancel one another, such that flow speed is insensitive to filament turnover, and shows simple dependence on motor activity and crosslink dynamics. These results provide a framework for understanding how animal cells tune cortical flow through local control of network remodeling.

## Author Summary

In this paper, we develop and analyze a minimal model for a 2D network of cross-linked actin filaments and myosin motors, representing the cortical cytoskeleton of eukaryotic cells. We implement coarse-grained representations of force production by myosin motors and stress dissipation through an effective cross-link friction and filament turnover. We use this model to characterize how the sustained production of active stress, and the steady dissipation of elastic stress, depend individually on motor activity, effective cross-link friction and filament turnover. Then we combine these results to gain insights into how microscopic network parameters control steady state flow produced by asymmetric distributions of motor activity. Our results provide a framework for understanding how local modulation of microscopic interactions within contractile networks control macroscopic quantities like active stress and effective viscosity to control cortical deformation and flow at cellular scales.

## Introduction

Cortical flow is a fundamental and ubiquitous form of cellular deformation that underlies cell polarization, cell division, cell crawling and multicellular tissue morphogenesis [1–6]. These flows originate within a thin layer of cross-linked actin filaments and myosin motors, called the actomyosin cortex, that lies just beneath the plasma membrane [7]. Local forces produced by bipolar myosin filaments are integrated

within cross-linked networks to build macroscopic contractile stress [8–10]. At the same time, cross-linked networks resist deformation and this resistance must be dissipated by network remodeling to allow macroscopic deformation and flow. How force production and dissipation depend on motor activity and network remodeling remains poorly understood.

One successful approach to modeling cortical flow has relied on coarse-grained phenomenological descriptions of actomyosin networks as active fluids, whose motions are driven by gradients of active contractile stress and opposed by an effectively viscous resistance [11]. In these models, spatial variation in active stress is typically assumed to reflect spatial variation in motor activity and force transmission [12], while viscous resistance is assumed to reflect the internal dissipation of elastic resistance due to local remodeling of filaments and/or cross-links [7, 13]. Models combining an active fluid description with simple kinetics for network assembly and disassembly, can successfully reproduce the spatiotemporal dynamics of cortical flow observed during polarization [11], cell division [14, 15], cell motility [16, 17] and tissue morphogenesis [18]. However, it remains a challenge to connect this coarse-grained description of cortical flow to the microscopic origins of force generation and dissipation within cross-linked actomyosin networks.

Studies in living cells reveal fluid-like stress relaxation on timescales of 10–100s [1, 2, 11, 19–21], which is thought to arise through a combination of cross link unbinding and actin filament turnover [7, 13, 22]. Theoretical [23, 24] and computational [25–27] studies reveal that cross-link unbinding can endow actin networks with complex time-dependent viscoelasticity. However, while cross-link unbinding is sufficient for viscous relaxation (creep) on very long timescales *in vitro*, it is unlikely to account for the rapid cortical deformation and flow observed in living cells [26, 28–31]. Experimental studies in living cells reveal rapid turnover of cortical actin filaments on timescales comparable to stress relaxation (10–100s) [32–36]. Perturbing turnover can lead to changes in cortical mechanics and in the rates and patterns of cortical flow [34, 37]. However, the specific contributions of actin turnover to stress relaxation and how these depend on network architecture remain unclear.

Recent work has also begun to reveal mechanisms for active stress generation in disordered actomyosin networks. Theoretical studies suggest that spatial heterogeneity in motor activity along individual filaments, and asymmetrical filament compliance (stiffer in extension than in compression), are sufficient for macroscopic contraction [38,39], although other routes to contractility may also exist [39]. Local interactions among actin filaments and myosin motors are sufficient to drive macroscopic contraction of disordered networks *in vitro* [40], and the kinematics of contraction observed in these studies support a mechanism based on asymmetrical filament compliance and filament buckling. However, in these studies, the filaments were preassembled and network contraction was transient, because of irreversible network collapse [41], or buildup of elastic resistance [42], or because network rearrangements (polarity sorting) dissipate the potential to generate contractile force [43–46]. This suggests that network turnover may play essential role(s) in allowing sustained production of contractile force. Recent theoretical and modeling studies have begun to explore how this might work [47–49], and to explore dynamic behaviors that can emerge when contractile material undergoes turnover [15,50]. However, it remains a challenge to understand how force production and dissipation depend individually on the local interplay of network architecture, motor activity and filament turnover, and how these dependencies combine to mediate tunable control of long range cortical flow.

Here, we construct and analyse a simple computational model that bridges between the microscopic description of cross-linked actomyosin networks and the coarse grained description of an active fluid. We represent actin filaments as simple springs with asymmetric compliance; we represent dynamic binding/unbinding of elastic cross-links as molecular friction [51–53] at filament crossover points; we represent motor activity as force coupling on a subset of filament cross-over points with a simple linear force/velocity relationship [54]. Finally, we model filament turnover by allowing entire filaments to appear with a fixed probability per unit area and disappear with fixed probabilities per unit time. We use this model first to characterize the passive response of a cross-linked network to externally applied stress, then the buildup and maintenance of active stress against an external resistance, and finally the steady state flows produced by an asymmetric distribution of active motors in which active stress and

passive resistance are dynamically balanced across the network. Our results reveal how network remodeling can tune cortical flow through simultaneous effects on active force generation and passive resistance to network deformation.

## Models

Our goal was to construct a minimal model that is detailed enough to capture essential microscopic features of cross-linked actomyosin networks (actin filaments with asymmetric compliance, dynamic cross-links, active motors and continuous filament turnover), but simple enough to explore, systematically, how these microscopic features control macroscopic deformation and flow. We focus on 2D networks because they capture a reasonable approximation of the quasi-2D cortical actomyosin networks that govern flow and deformation in many eukaryotic cells [11,55], or the quasi-2D networks studied recently *in vitro* [40,56].

Fig. 1 provides a schematic overview of our model's assumptions. We model each filament as an oriented elastic spring with relaxed length  $l_s$ . The state of a filament is defined by the positions of its endpoints  $\mathbf{x}_i$  and  $\mathbf{x}_{i+1}$  marking its (-) and (+) ends respectively. The index  $i$  enumerates over all endpoints of all filaments. We refer to the filament connecting endpoint  $i$  and  $i+1$  as filament  $i$ , and we define  $\hat{\mathbf{u}}_i$  to be the unit vector oriented along filament  $i$  from endpoint  $i$  to endpoint  $i+1$ .

### Asymmetric filament compliance

We assume (Fig. 1A) that local deformation of filament  $i$  gives rise to an elastic force:

$$\mathbf{F}_{i,i+1}^\mu = \mu \gamma_i \hat{\mathbf{u}}_i \tag{1}$$

where  $\gamma_i = (|\mathbf{x}_{i-1} - \mathbf{x}_i| - l_s)/l_s$  is the strain on filament  $i$ , and the elastic modulus  $\mu$  is a composite quantity that represents both filament and cross-linker compliance as in the effective medium theory of Broederz and colleagues [57]. To model asymmetric filament compliance, we set  $\mu = \mu_e$  if the strain is positive (extension), and  $\mu = \mu_c$  if the strain is negative (compression). The total elastic force on a filament endpoint  $\mathbf{i}$  can be written as:

$$\mathbf{F}_i^{\text{elas}} = \mathbf{F}_{i,i+1}^\mu - \mathbf{F}_{i-1,i}^\mu \quad (2)$$

In the limit of highly rigid cross-links and flexible filaments, our model approaches the pure semi-flexible filament models of [58, 59]. In the opposite limit (nearly rigid filaments and highly flexible cross links), our model approaches that of [57] in small strain regimes before any nonlinear cross link stiffening.

### Drag-like coupling between overlapping filaments

Previous models represent cross-linkers as elastic connections between pairs of points on neighboring filaments that appear and disappear with either fixed or force-dependent probabilities [25, 57]. Here, we introduce a coarse-grained representation of crosslink dynamics by introducing an effective drag force that couples every pair of overlapping filaments, and which represents a molecular friction arising from the time-averaged contributions of many individual transient crosslinks (Fig. 1B). This coarse-grained approximation has been shown to be adequate in the case of ionic cross-linking of actin [60, 61], and has been used to justify simple force-velocity curves for myosin bound filaments in other contexts [54].

To implement coupling through effective drag, for any pair of overlapping filaments  $j$  and  $k$ , we write the drag force on filament  $j$  as:

$$\mathbf{F}_{j,k}^\xi = -\xi(\mathbf{v}_j - \mathbf{v}_k) \quad (3)$$

where  $\xi$  is the drag coefficient and  $\mathbf{v}_j, \mathbf{v}_k$  are the average velocities of filaments  $j$  and  $k$ . We apportion this drag force to the two endpoints ( $j, j+1$ ) of filament  $j$  as follows: If  $\mathbf{x}_{j,k}$  is the position of the filament overlap, then we assign  $(1 - \lambda_{j,k})\mathbf{F}_{j,k}^\xi$  to endpoint  $j$  and  $\lambda_{j,k}\mathbf{F}_{j,k}^\xi$  to endpoint  $j+1$ , where  $\lambda_{j,k} = |\mathbf{x}_{j,k} - \mathbf{x}_j|/|\mathbf{x}_{j+1} - \mathbf{x}_j|$ .

The total crosslink coupling force on endpoint  $i$  due to overlaps along filament  $i$  and  $i-1$  can then be written:

$$\mathbf{F}_i^{\text{xl}} = \sum_j (1 - \lambda_{i,j})\mathbf{F}_{i,j}^\xi + \sum_k \lambda_{i-1,k}\mathbf{F}_{i-1,k}^\xi \quad (4)$$

where the sums are taken over all filaments  $j$  and  $k$  that overlap with filaments  $i$  and

i-1 respectively.

This model assumes a linear relation between the drag force and the velocity difference between attached filaments. Although non-linearities can arise through force dependent detachment kinetics and/or non-linear force extension of cross-links, we assume here that these non-linear effects are of second or higher order.

### Active coupling for motor driven filament interactions

To add motor activity at the point of overlap between two filaments  $j$  and  $k$ ; for each filament in the pair, we impose an additional force of magnitude  $v$ , directed towards its (-) end (Fig. 1C):

$$\mathbf{F}_i^v = -v\hat{\mathbf{u}}_i \quad (5)$$

and we impose an equal and opposite force on its overlapping partner. We distribute these forces to filament endpoints as described above for crosslink coupling forces. Thus, the total force on endpoint  $i$  due to motor activity can be written as:

$$\mathbf{F}_i^{\text{motor}} = v \sum_j (1 - \lambda_{i,j}) (\hat{\mathbf{u}}_i - \hat{\mathbf{u}}_j) q_{i,j} + v \sum_k (\lambda_{i-1,k}) (\hat{\mathbf{u}}_{i-1} - \hat{\mathbf{u}}_k) q_{i-1,k} \quad (6)$$

where  $j$  and  $k$  enumerate over all filaments that overlap with filaments  $i$  and  $i-1$  respectively, and  $q_{j,k}$  equals 0 or 1 depending on whether there is an “active” motor at this location. To model dispersion of motor activity, we set  $q_{i,j} = 1$  on a randomly selected subset of filament overlaps, such that  $\bar{q} = \phi$ , where  $\bar{q}$  indicates the mean of  $q$  (Fig. 1C).

### Equations of motion

To write the full equation of motion for a network of actively and passively coupled elastic filaments, we assume the low Reynold’s number limit in which inertial forces can be neglected, and we equate the sum of all forces acting on each filament endpoint to zero to obtain:

$$0 = -l_s \zeta \mathbf{v}_i - \mathbf{F}_i^{\text{xl}} + \mathbf{F}_i^{\text{elas}} + \mathbf{F}_i^{\text{motor}} \quad (7)$$

where the first term represents the hydrodynamic drag on the half-filament adjoining endpoint  $i$  with respect to motion against the surrounding fluid, and  $\zeta$  is the drag coefficient.

## 2D network formation

We used a mikado model approach [62] to initialize a minimal network of overlapping unstressed linear filaments in a rectangular 2D domain. We generate individual filaments by laying down straight lines, of length  $L$ , with random position and orientation. We define the density using the average distance between cross-links along a filament,  $l_c$ . A simple geometrical argument can then be used to derive the number of filaments filling a domain as a function of  $L$  and  $l_c$  [58]. Here, we use the approximation that the number of filaments needed to tile a rectangular domain of size  $D_x \times D_y$  is  $2D_x D_y / L l_c$ , and that the length density is therefore simply,  $2/l_c$ .

## Modeling filament turnover

In living cells, actin filament assembly is governed by multiple factors that control filament nucleation, branching and elongation. Likewise filament disassembly is governed by multiple factors that promote filament severing and monomer dissociation at filament ends. Here, we implement a very simple model for filament turnover in which entire filaments appear with a fixed rate per unit area,  $k_{app}$  and disappear at a rate  $k_{diss}\rho$ , where  $\rho$  is a filament density (Fig. 1D). With this assumption, in the absence of network deformation, the density of filaments will equilibrate to a steady state density,  $k_{app}/k_{diss}$ , with time constant  $\tau_r = 1/k_{diss}$ . In deforming networks, the density will be set by a competition between strain thinning ( $\gamma > 0$ ) or thickening ( $\gamma < 0$ ), and density equilibration via turnover. To implement this model, at fixed time intervals  $\tau_s < 0.01 \cdot \tau_r$  (i.e. 1% of the equilibration time), we selected a fraction,  $\tau_s/\tau_r$ , of existing filaments (i.e. less than 1% of the total filaments) for degradation. We then generated a fixed number of new unstrained filaments  $k_{app}\tau_s D_x D_y$  at random positions and orientations within the original domain. We refer to  $k_{diss} = 1/\tau_r$  as the turnover rate, and to  $\tau_r$  as the turnover time.

## Simulation methods

Further details regarding our simulation approach and references to our code can be found in the Supplementary Information (S1 Appendix A.1). Briefly, equations 1-7 define a coupled system of ordinary differential equations that can be written in the form:

$$\mathbf{A} \cdot \dot{\mathbf{x}} = \mathbf{f}(\mathbf{x}) \quad (8)$$

where  $\mathbf{x}$  is a vector of filament endpoint positions,  $\dot{\mathbf{x}}$  the endpoint velocities,  $\mathbf{A}$  is a matrix with constant coefficients that represent crosslink coupling forces between overlapping filaments, and  $\mathbf{f}(\mathbf{x})$  represents the active (motor) and elastic forces on filament endpoints. We smoothed all filament interactions, force fields, and constraints linearly over small regions such that the equations contained no sharp discontinuities. We numerically integrate this system of equations to find the time evolution of the positions of all filament endpoints. We generate a network of filaments with random positions and orientations as described above within a domain of size  $D_x$  by  $D_y$ . For all simulations, we imposed periodic boundaries in the  $y$ -dimension. To impose an extensional stress, we constrained all filament endpoints within a fixed distance  $0.05 \cdot D_x$  from the left edge of the domain to be non-moving, then we imposed a rightwards force on all endpoints within a distance  $0.05 \cdot D_x$  from the right edge of the domain. To simulate free contraction, we removed all constraints at domain boundaries; to assess buildup and maintenance of contractile stress under isometric conditions, we used periodic boundary conditions in both  $x$  and  $y$  dimensions.

We measured the local velocity of the network at different positions along the axis of deformation as the mean velocity of all filaments intersecting that position; we measured the internal network stress at each axial position by summing the axial component of the tensions on all filaments intersecting that position, and dividing by network height; finally, we measured network strain rate as the average of all filament velocities divided by their positions.

We assigned biological plausible reference values for all parameters (See Table 1). For individual analyses, we sampled the ranges of parameter values around these reference values shown in S1 Table.

**Table 1.** Simulation parameters with reference values

Parameter	Symbol	Reference Value
extensional modulus	$\mu_e$	$1nN$
compressional modulus	$\mu_c$	$0.01nN$
cross-link drag coefficient	$\xi$	<i>unknown</i>
solvent drag coefficient	$\zeta$	$0.0005 \frac{nNs}{\mu m^2}$
filament length	$L$	$5\mu m$
cross-link spacing	$l_c$	$0.5\mu m$
active filament force	$v$	$0.1nN$
active cross-link fraction	$\phi$	$0.1 < 0.9$
domain size	$D_x \times D_y$	$20 \times 50\mu m$

## Results

The goal of this study is to understand how cortical flow is shaped by the simultaneous dependencies of active stress and effective viscosity on filament turnover, crosslink drag and on “network parameters” that control filament density, elasticity and motor activity. We approach this in three steps: First, we analyze the passive deformation of a cross-linked network in response to an externally applied stress; we identify regimes in which the network response is effectively viscous and characterize the dependence of effective viscosity on network parameters and filament turnover. Second, we analyze the buildup and dissipation of active stress in cross-linked networks with active motors, as they contract against an external resistance; we identify conditions under which the network can produce sustained stress at steady state, and characterize how steady state stress depends on network parameters and filament turnover. Finally, we confirm that the dependencies of active stress and effective viscosity on network parameters and filament turnover are sufficient to predict the dynamics of networks undergoing steady state flow in response to spatial gradients of motor activity.

### Filament turnover allows and tunes effectively viscous steady state flow.

**Networks with passive cross-links and no filament turnover undergo three stages of deformation in response to an extensional force.** To characterize the passive response of a cross-linked filament network without filament recycling, we simulated a simple uniaxial strain experiment in which we pinned the network at one end, imposed an external stress at the opposite end, and then quantified network strain

and internal stress as a function of time (Fig. 1E). The typical response occurred in three qualitatively distinct phases (Fig. 2A,C). At short times the response was viscoelastic, with a rapid buildup of internal stress and a rapid  $\sim$ exponential approach to a fixed strain (S1 FigA), which represents the elastic limit in the absence of cross-link slip predicted by [58]. At intermediate times, the local stress and strain rate were approximately constant across the network (Fig. 2B), and the response was effectively viscous; internal stress remained constant while the network continued to deform slowly and continuously with nearly constant strain rate (shown as dashed line in Fig. 2C) as filaments slip past one another against the effective cross-link drag. In this regime, we can quantify effective viscosity,  $\eta_c$ , as the ratio of applied stress to the measured strain rate. Finally, as the network strain approached a critical value ( $\sim 30\%$  for the simulation in Fig. 2), strain thinning lead to decreased network connectivity, local tearing, and rapid acceleration of the network deformation (see inset in Fig. 2C).

**Network architecture sets the rate and timescales of deformation.** To characterize how effective viscosity and the timescale for transition to effectively viscous behavior depend on network architecture and cross-link dynamics, we simulated a uniaxial stress test, holding the applied stress constant, while varying filament length  $L$ , density  $l_c$ , elastic modulus  $\mu_e$  and cross link drag  $\xi$  (see S1 Table). We measured the elastic modulus,  $G_0$ , the effective viscosity,  $\eta_c$ , and the timescale  $\tau_c$  for transition from viscoelastic to effectively viscous behavior, and compared these to theoretical predictions. We observed a transition from viscoelastic to effectively viscous deformation for the entire range of parameter values that we sampled. Our estimate of  $G_0$  from simulation agreed well with the closed form solution  $G_0 \sim \mu/l_c$  predicted by a previous theoretical model [58] for networks of semi-flexible filaments with irreversible cross-links (Fig. 3B).

A simple theoretical analysis of filament networks with frictional cross link slip, operating in the intermediate viscous regime (see S1 Appendix A.2), predicted that the effective viscosity  $\eta_c$  should be proportional to the cross-link drag coefficient and to the square of the number of cross-links per filament:

$$\eta_c = 4\pi\xi \left( \frac{L}{l_c} - 1 \right)^2 \tag{9}$$

As shown in Fig. 3B, our simulations agree well with this prediction for a large range of sampled network parameters. Finally, for many linear viscoelastic materials, the ratio of effective viscosity to the elastic modulus  $\eta_c/G_0$  sets the timescale for transition from elastic to viscous behavior [63]. Combining our approximations for  $G_0$  and  $\eta_c$ , we predict a transition time,  $\tau_c \approx L^2\xi/l_c\mu$ . Measuring the time at which the strain rate became nearly constant (i.e.  $\gamma \sim t^n$  with  $n > 0.8$ ) yields an estimate of  $\tau_c$  that agrees well with this prediction over the entire range of sampled parameters (Fig. 3C). Thus the passive response of filament networks with frictional cross link drag is well-described on short (viscoelastic) to intermediate (viscous) timescales by an elastic modulus  $G_0$ , an effective viscosity  $\eta_c$ , and a transition timescale  $\tau_c$ , with well-defined dependencies on network parameters. However, without filament turnover, strain thinning and network tearing limits the extent of viscous deformation to small strains.

**Filament turnover allows sustained large-scale viscous flow and defines two distinct flow regimes.** To characterize how filament turnover shapes the passive network response to an applied force, we introduced a simple form of turnover in which entire filaments disappear at a rate  $k_{diss}\rho$ , where  $\rho$  is the filament density, and new unstrained filaments appear with a fixed rate per unit area,  $k_{app}$ . In a non-deforming network, filament density will equilibrate to a steady state value,  $\rho_0 = k_{ass}/k_{diss}$ , with time constant  $\tau_r = 1/k_{diss}$ . However, in networks deforming under extensional stress, the density will be set by a competition between strain thinning and density equilibration via turnover.

We simulated a uniaxial stress test for different values of  $\tau_r$ , while holding all other parameters fixed (Fig. 4A-C). For large  $\tau_r$ , as described above, the network undergoes strain thinning and ultimately tears. Decreasing  $\tau_r$  increases the rate at which the network equilibrates towards a steady state density  $\rho_0$ . However, it also increases the rate of deformation and thus the rate of strain thinning (Fig. 4B). We found that the former effect dominates, such that below a critical value  $\tau_r = \tau_{crit}$ , the network can achieve a steady state characterized by a fixed density and a constant strain rate (S2 Fig). Simple calculations (S1 Appendix A.3) show that the critical value of  $\tau_r$  is approximately:

$$\tau_{crit} = \frac{\xi \left( \sqrt{\frac{L}{l_c}} - 1 \right)^3}{\sigma} \quad (10)$$

where  $\sigma$  is the applied stress,  $L/l_c$  the linear cross link density, and  $\xi$  is the effective crosslink drag.

For  $\tau_r < \tau_{crit}$ , we observed two distinct steady state flow regimes (Fig. 4B,C). For intermediate values of  $\tau_r$ , effective viscosity remains constant with decreasing  $\tau_r$ . However, below a certain value of  $\tau_r$  ( $\approx 10^3$  for the parameters used in Fig. 4C), effective viscosity decreased monotonically with further decreases in  $\tau_r$ . To understand what sets the timescale for transition between these two regimes, we measured effective viscosity at steady state for a wide range of network parameters ( $L, \mu, l_c$ ), crosslink drags ( $\xi$ ) and filament turnover times (Fig. 4D). Strikingly, when we plotted the normalized effective viscosity  $\eta_r/\eta_c$  vs a normalized recycling rate  $\tau_r/\tau_c$  for all parameter values, the data collapsed onto a single curve, with a transition at  $\tau_r \approx \tau_c$  between an intermediate turnover regime in which effective viscosity is independent of  $\tau_r$  and an high turnover regime in which effective viscosity falls monotonically with decreasing  $\tau_r/\tau_c$  (Fig. 4D).

This biphasic dependence of effective viscosity on filament turnover can be understood intuitively as follows: As new filaments are born, they become progressively stressed as they stretch and reorient under local influence of surrounding filaments, eventually reaching an elastic limit where their contribution to resisting network deformation is determined by effective crosslink drag. The time to reach this limit is about the same as the time,  $\tau_c$ , for an entire network of initially unstrained filaments to reach an elastic limit during the initial viscoelastic response to uniaxial stress, as shown in Fig. 2b. For  $\tau_r < \tau_c$ , individual filaments do not have time, on average, to reach the elastic limit before turning over; thus the deformation rate is determined by the elastic resistance of partially strained filaments, which increases with lifetime up to  $\tau_r = \tau_c$ . For  $\tau_r > \tau_c$ , the deformation rate is largely determined by cross-link resistance to sliding of maximally strained filaments, and the effective viscosity is insensitive to further increase in  $\tau_r$ .

These results complement and extend a previous computational study of irreversibly cross-linked networks of treadmilling filaments deforming under extensional stress [64].

Kim et al identified two regimes of effectively viscous deformation: a “stress-dependent” regime in which filaments turnover before they become strained to an elastic limit and deformation rate is proportional to both applied stress and turnover rate; and a “stress-independent” regime in which filaments reach an elastic limit before turning over and deformation rate depends only on the turnover rate. The fast and intermediate turnover regimes that we observe here correspond to the stress-dependent and independent regimes described by Kim et al, but with a key difference. Without filament turnover, Kim et al’s model predicts that a network cannot deform beyond its elastic limit. In contrast, our model predicts viscous flow at low turnover, governed by an effective viscosity that is set by cross-link density and effective drag. Thus our model provides a self-consistent framework for understanding how crosslink unbinding and filament turnover contribute separately to viscous flow and connects these contributions directly to previous theoretical descriptions of cross-linked networks of semi-flexible filaments.

In summary, our simulations predict that filament turnover allows networks to undergo viscous deformation indefinitely, without tearing, over a wide range of different effective viscosities and deformation rates. For  $\tau_r < \tau_{crit}$ , this behavior can be summarized by an equation of the form:

$$\eta = \frac{\eta_c}{1 + (\tau_c/\tau_r)^m} \quad (11)$$

For  $\tau_r \gg \tau_c$ ,  $\eta \approx \eta_c$ : effective viscosity depends on crosslink density and effective crosslink drag, independent of changes in recycling rate. For  $\tau_r \ll \tau_c$ , effective viscosity is governed by the level of elastic stress on network filaments, and becomes strongly dependent on filament lifetime:  $\eta \sim \eta_c(\tau_r/\tau_c)^m$ . The origins of the  $m = 3/4$  scaling remains unclear (see Discussion).

## Filament turnover allows persistent stress buildup in active networks

**In the absence of filament turnover, active networks with free boundaries contract and then stall against passive resistance to network compression.**

Previous work [38,40,65] identifies asymmetric filament compliance and spatial

heterogeneity in motor activity as minimal requirements for macroscopic contraction of disordered networks. To confirm that our simple implementation of these two requirements (see Models section) is sufficient for macroscopic contraction, we simulated active networks that are unconstrained by external attachments, varying filament length, density, crosslink drag and motor activity. We observed qualitatively similar results for all choices of parameter values: Turning on motor activity in an initially unstrained network induced rapid initial contraction, followed by a slower buildup of compressive stress (and strain) on individual filaments, and an  $\sim$ exponential approach to stall (Fig. 5). The time to stall,  $\tau_s$ , scaled as  $L\xi/v$  (S3 FigA). On even longer timescales, polarity sorting of individual filaments, as previously described [42,44–46] lead to network expansion (see S2 Video).

During the rapid initial contraction, the increase in network strain closely matched the increase in mean compressive strain on individual filaments Fig. 5B, as predicted theoretically [38,39] and observed experimentally [40]. Contraction required asymmetric filament compliance and spatial heterogeneity of motor activity ( $\mu_e/\mu_c > 1$ ,  $\phi < 1$ , S3 FigB). Thus our model captures a minimal mechanism for bulk contractility in disordered networks through asymmetric filament compliance and dispersion of motor activity. However, in the absence of turnover, contraction is limited by internal buildup of compressive resistance and the dissipative effects of polarity sorting.

**Active networks cannot sustain stress against a fixed boundary in the absence of filament turnover.** During cortical flow, regions with high motor activity contract against a passive resistance from neighboring regions with lower motor activity. To understand how the active stresses that drive cortical flow are shaped by motor activity and network remodeling, we analyzed the buildup and maintenance of contractile stress in active networks contracting against a rigid boundary. We simulated active networks contracting from an initially unstressed state against a fixed boundary (Fig. 6A,B), and monitored the time evolution of mean extensional (blue), compressional (red) and total (black) stress on network filaments (Fig. 6C,D). We focused initially on the scenario in which there is no, or very slow, filament turnover, sampling a range of parameter values controlling filament length and density, motor activity, and crosslink drag.

We observed a similar behavior in all cases: total stress built rapidly to a peak value  $\sigma_m$ , and then decayed towards zero (Fig. 6C,D). The rapid initial increase in total stress was determined largely by the rapid buildup of extensional stress (Fig. 6C,D) on a subset of network filaments (Fig. 6A,B  $t = 10s$ ). The subsequent decay involved two different forms of local remodeling: under some conditions, e.g. for higher motor activity (e.g. Fig. 6A,C), the decay was associated with rapid local tearing and fragmentation, leading to global loss of network connectivity as described previously both in simulations [48] and *in vitro* experiments [41]. However, for many parameters, (e.g. for higher motor activity as in Fig. 6B,D), the decay in stress occurred with little or no loss of global connectivity. Instead, local filament rearrangements changed the balance of extensile vs compressive forces along individual filaments, leading to a slow decrease in the average extensional stress, and a correspondingly slow increase in the compressional stress, on individual filaments (see Fig. 6D).

Combining dimensional analysis with trial and error, we were able to find empirical scaling relationships describing the dependence of maximum stress  $\sigma_m$  and the time to reach maximum stress  $\tau_m$  on network parameters and effective crosslink drag ( $\sigma_m \sim \sqrt{\mu_e v}/l_c$ ,  $\tau_m \sim L\xi/\sqrt{\mu_e v}$ , S3 FigC,D). Although these relationships should be taken with a grain of salt, they are reasonably consistent with our simple intuition that the peak stress should increase with motor force ( $v$ ), extensional modulus ( $\mu_e$ ) and filament density ( $1/l_c$ ), and the time to reach peak stress should increase with crosslink drag ( $\xi$ ) and decrease with motor force ( $v$ ) and extensional modulus ( $\mu_e$ ).

**Filament turnover allows active networks to exert sustained stress on a fixed boundary.** Regardless of the exact scaling dependencies of  $\sigma_m$  and  $\tau_m$  on network parameters, these results reveal a fundamental limit on the ability of active networks to sustain force against an external resistance in the absence of filament turnover. To understand how this limit can be overcome by filament turnover, we simulated networks contracting against a fixed boundary from an initially unstressed state, for increasing rates of filament turnover (decreasing  $\tau_r$ ), while holding all other parameter values fixed (Fig. 7A-C). While the peak stress decreased monotonically with decreasing  $\tau_r$ , the steady state stress showed a biphasic response, increasing initially with decreasing  $\tau_r$ , and then falling off as  $\tau_r \rightarrow 0$ . We observed a biphasic response

regardless of how stress decays in the absence of turnover, i.e. whether decay involves loss of network connectivity, or local remodeling without loss of connectivity, or both (S4 Fig and not shown). Significantly, when we plot normalized steady state stress ( $\sigma/\sigma_m$ ) vs normalized recycling time ( $\tau_r/\tau_m$ ) for a wide range of network parameters, the data collapse onto a single biphasic response curve, with a peak near  $\tau_r/\tau_m = 1$  (Fig. 7D). In particular, for  $\tau_r < \tau_m$ , the scaled data collapsed tightly onto a single curve representing a linear increase in steady state stress with increasing  $\tau_r$ . For  $\tau_r > \tau_m$ , the scaling was less consistent, although the trend towards a monotonic decrease with increasing  $\tau_r$  was clear. These results reveal that filament turnover can “rescue” the dissipation of active stress during isometric contraction due to network remodeling, and they show that, for a given choice of network parameters, there is an optimal choice of filament lifetime that maximizes steady state stress.

We can understand the biphasic dependence of steady state stress on filament lifetime using the same reasoning applied to the case of passive flow: During steady state contraction, the average filament should build and dissipate active stress on approximately the same schedule as an entire network contracting from an initially unstressed state (Fig. 7B). Therefore for  $\tau_r < \tau_m$ , increasing lifetime should increase the mean stress contributed by each filament. For  $\tau_r > \tau_m$ , further increases in lifetime should begin to reduce the mean stress contribution. Directly comparing the time-dependent buildup and dissipation of stress in the absence of turnover, with the dependence of steady state stress on  $\tau_r$ , supports this interpretation (S5 Fig)

As for the passive response (i.e. Equation 11), we can describe this biphasic dependence phenomenologically with an equation of the form:

$$\sigma_{ss} = \frac{\sigma_m}{(\tau_r/\tau_m)^n + \tau_m/\tau_r} \quad (12)$$

where the origins of the exponent  $n$  remain unclear.

## Filament turnover tunes the balance between active stress buildup and viscous stress relaxation to generate flows

Thus far, we have considered independently how network remodeling controls the passive response to an external stress, or the steady state stress produced by active

contraction against an external resistance. We now consider how these two forms of dependence will combine to shape steady state flow produced by spatial gradients of motor activity. We consider a simple scenario in which a network is pinned on either side and motor activity is continuously patterned such that the right half network has uniformly high levels of motor activity (controlled by  $v$ , with  $\psi = 0.5$ ), while the left half network has none. Under these conditions, the right half network will contract continuously against a passive resistance from the left half network. Because of asymmetric filament compliance, the internal resistance of the right half network to active compression should be negligible compared to the external resistance of the left half network. Thus the steady state flow will be described by:

$$\dot{\gamma} = \frac{\sigma_{ss}}{\eta} \tag{13}$$

where  $\sigma_{ss}$  is the active stress generated by the right half-network (less the internal resistance to filament compression),  $\eta$  is the effective viscosity of the left half network and strain rate  $\dot{\gamma}$  is measured in the left half-network. Note that strain rate can be related to the steady state flow velocity  $v$  at the boundary between right and left halves through  $v = \dot{\gamma}Dx$ . Therefore, we can understand the dependence of flow speed on filament turnover and other parameters using the approximate relationships summarized by equations 11 and 12 for  $\eta$  and  $\sigma_{ss}$ . As shown in Fig. 8, there are two qualitatively distinct possibilities for the dependence of strain rate on  $\tau_r$ , depending on the relative magnitudes of  $\tau_m$  and  $\tau_c$ . In both cases, for fast enough turnover ( $\tau_r < \min(\tau_m, \tau_c)$ ), we expect weak dependence of strain rate on  $\tau_r$  ( $\dot{\gamma} \sim \tau_r^{1/4}$ ). For all parameter values that we sampled in this study (which were chosen to lie in a physiological range),  $\tau_m > \tau_c$ . Therefore we predict the dependence of steady state strain rate on  $\tau_r$  shown in Fig. 8A.

To confirm this prediction, we simulated the simple scenario described above for a range of values of  $\tau_r$ , with all other parameter values initially fixed. As expected, we observed a sharp dependence of steady state flow speeds on filament recycling rate (Fig. 9B,C). For very long recycling times, ( $\tau_r = 1000s$ , dark blue line), there was a rapid initial deformation (contraction of the active domain and dilation of the passive domain), followed by a slow approach to a steady state flow characterized by slow contraction of the right half-domain and a matching dilation of the left half-domain (see

S6 Fig). However, with decreasing values of  $\tau_r$ , steady state flow speeds increased steadily, before reaching an approximate plateau on which flow speeds varied by less than 15 % over more than two decades of variation in  $\tau_r$  (Fig. 9C).

We repeated these simulations for a wider range of parameter values, and saw similar dependence of  $\dot{\gamma}$  on  $\tau_r$  in all cases. Using equation 11 with  $\tau_r < \tau_c$  and equation 12 with  $\tau_r < \tau_m$ , and the theoretical or empirical scaling relationships found above for  $\eta_c$ ,  $\tau_c$ ,  $\sigma_m$  and  $\tau_m$ , we predict a simple scaling relationship for  $\dot{\gamma}$  (for small  $\tau_r$ ):

$$\dot{\gamma} = \frac{v}{\xi L} (\tau_r)^{1/4} \quad (14)$$

Indeed, when we plot the steady state measurements of  $\dot{\gamma}$ , normalized by  $v/\xi L$ , for all parameter values, the data collapse onto a single curve for small  $\tau_r$ . Thus, our simulations identify a flow regime, characterized by sufficiently fast filament turnover, in which the steady state flow speed is buffered against variation in turnover, and has a relatively simple dependence on other network parameters.

## Discussion

Cortical flows are shaped by the dynamic interplay of force production and dissipation within cross-linked actomyosin networks. Here we combined computational models with simple theoretical analyses to explore how this interplay depends on filament turnover, crosslink dynamics and network architecture. Our results reveal an essential requirement for filament turnover during cortical flow, both to sustain active stress and to continuously relax elastic resistance without catastrophic loss of network connectivity. Moreover, we find that biphasic dependencies of active stress and passive relaxation on filament lifetime define multiple regimes for steady state flow with distinct dependencies on network parameters and filament turnover.

We identify two regimes of passive response to external stress: a low turnover regime in which filaments strain to an elastic limit before turning over, and effective viscosity depends on crosslink density and effective crosslink friction, and a high turnover regime in which filaments turn over before reaching an elastic limit and effective viscosity is proportional to elastic resistance and  $\sim$ proportional to filament lifetime. Thus our

model captures the qualitatively distinct contributions of transient crosslinks and filament turnover within a single self-consistent framework. We note that the weakly sub-linear dependence of effective viscosity on filament lifetime that we observe here may simply reflect a failure to capture very local modes of filament deformation, since a previous study [64] in which filaments were represented as connected chains of smaller segments predicted linear dependence of effective viscosity on filament lifetime.

Our simulations active networks confirm the theoretical prediction [38, 40, 65] that spatial heterogeneity of motor activity and asymmetric filament compliance are sufficient to support macroscopic contraction of unconstrained networks. However, under isometric conditions, and without filament turnover, our simulations predict that active stress cannot be sustained. On short timescales, motor forces drive local buildup of extensional stress, but on longer timescales, local motor-driven filament rearrangements and thus local changes in connectivity, invariably lead to a decay in active stress. Under some conditions, contractile forces drive networks towards a critically connected state, leading to tearing and fragmentation, as previously described [41, 48]. However, we find that stress decay can also occur without any global loss of connectivity, through a gradual decrease in extensile force and a gradual increase in compressive force along individual filaments. When filaments can slide relative to one another, the motor forces that produce active stress will inevitably lead to local changes in connectivity that decrease active stress. These results suggest that for contractile networks to maintain isometric tension on long timescales, they must either form stable crosslinks to prevent filament rearrangements, or they must continuously recycle network filaments (or active motors) to renew the local potential for production of active stress.

Indeed, our simulations predict that filament turnover is sufficient for maintenance of active stress and they predict a biphasic dependence of steady state stress on filament turnover: For short-lived filaments ( $\tau_r < \tau_m$ ), steady state stress increases linearly with filament lifetime because filaments have more time to build towards peak extensional stress before turning over. For longer lived filaments ( $\tau_r > \tau_m$ ), steady state stress decreases monotonically with filament lifetime because local rearrangements decrease the mean contributions of longer lived filaments. These findings imply that for cortical

networks that sustain contractile stress under approximately isometric conditions, tuning filament turnover can control the level of active stress, and there will be an optimal turnover rate that maximizes the stress, all other things equal. This may be important, for example in early development, where contractile forces produced by cortical actomyosin networks play key roles in maintaining, or controlling slow changes in cell shape and tissue geometry [7, 14, 66].

For cortical networks that undergo steady state flows driven by spatial gradients of motor activity, our simulations predict that the biphasic dependencies of steady state stress and effective viscosity on filament lifetime define multiple regimes of steady state flow, characterized by different dependencies on filament turnover (and other network parameters). In particular, the  $\sim$ linear dependencies of steady state stress and effective viscosity on filament lifetime for short-lived filaments define a fast turnover regime in which steady state flow speeds are buffered against variations in filament lifetime, and are predicted to depend in a simple way on motor activity and crosslink resistance. Measurements of F-actin turnover times in cells that undergo cortical flow [32, 67–71] suggests that they may indeed operate in this fast turnover regime, and recent studies in *C. elegans* embryos suggests that cortical flow speeds are surprisingly insensitive to depletion of factors (ADF/Cofilin) that govern filament turnover [11], consistent with our model's predictions. Stronger tests of our model's predictions will require more systematic analyses of how flow speeds vary with filament and crosslink densities, motor activities, and filament lifetimes.

## Supporting Information

**S1 Appendix. Code Reference and Supplementary Methods A.1)** Reference to simulation and analysis code. **A.2)** Derivation of effective viscosity. **A.3)** Derivation of critical turnover timescale for steady state flow

**S1 Table. Parameter values.** List of parameter values used for each set of simulations.

**S1 Fig. Fast viscoelastic response to extensional stress.** Plots of normalized strain vs time during the elastic phase of deformation in passive networks under extensional stress. Measured strain is normalized by the equilibrium strain predicted for a network of elastic filaments without crosslink slip  $\gamma_{eq} = \sigma/G_0 = \sigma/(2\mu/l_c)$ .

**S2 Fig. Filament turnover rescues strain thinning.** **A)** Plots of strain vs time for different turnover times (see inset in (b)). Note the increase in strain rates with decreasing turnover time. **B)** Plots of filament density vs strain for different turnover times  $\tau_r$ . For intermediate  $\tau_r$ , simulations predict progressive strain thinning, but at a lower rate than in the complete absence of recycling. For higher  $\tau_r$ , densities approach steady state values at longer times.

**S3 Fig. Mechanical properties of active networks.** **A)** Time for freely contracting networks to reach maximum strain,  $\tau_s$ , scales with  $L\xi/v$ . **B)** Free contraction requires asymmetric filament compliance, and total network strain increases with the applied myosin force  $v$ . Note that the maximum contraction approaches an asymptotic limit as the stiffness asymmetry approaches a ratio of  $\sim 100$ . **C)** Maximum stress achieved during isometric contraction,  $\sigma_m$ , scales approximately with  $\sqrt{\mu_e v}/l_c$ . **D)** Time to reach max stress during isometric contraction scales approximately with  $L\xi/\sqrt{\mu_e v}$ . Scalings for  $\tau_s$ ,  $\sigma_m$  and  $\tau_m$  were determined empirically by trial and error, guided by dimensional analysis.

**S4 Fig. Filament turnover prevents tearing of active networks.** Plots of normalized strain vs time during the elastic phase of deformation in passive networks under extensional stress. Measured strain is normalized by the equilibrium strain predicted for a network of elastic filaments without crosslink slip  $\gamma_{eq} = \sigma/G_0 = \sigma/(2\mu/l_c)$ .

**S5 Fig. Bimodal dependence on turnover time matches bimodal buildup and dissipation of stress in the absence of turnover.** **A)** Bimodal buildup of stress in a network with very slow turnover ( $\tau_r = 1000s$ ). **B)** Steady state stress for networks with same parameters as in (a), but for a range of filament turnover times.

**S6 Fig. Dynamics of steady state flow.** Plots of stress and strain vs position for networks in which motor activity is limited to the right-half domain and filament turnover time is either **A)**  $\tau_r = 10000$  or **B)**  $\tau_r = 10s$ . Blue indicates velocity while orange represents total stress, measured as described in the main text.

**S1 Video. Extensional strain in passive networks.** Movie of simulation setup shown in Fig. 2. Colors are the same as in figure.

**S2 Video. Active networks contracting with free boundaries.** Movie of simulation setup shown in Fig. 5. Colors are the same as in figure.

## Acknowledgments

We would like to thank Shiladitya Banerjee for stimulating discussions.

## References

1. Bray D, White J. Cortical flow in animal cells. *Science*. 1988;239(4842):883–888. Available from: <http://www.sciencemag.org/content/239/4842/883.abstract>.
2. Hird SN, White JG. Cortical and cytoplasmic flow polarity in early embryonic cells of *Caenorhabditis elegans*. *The Journal of Cell Biology*. 1993;121(6):1343–1355. Available from: <http://jcb.rupress.org/content/121/6/1343.abstract>.
3. Benink HA, Mandato CA, Bement WM. Analysis of Cortical Flow Models In Vivo. *Molecular Biology of the Cell*. 2000 08;11(8):2553–2563. Available from: <http://www.ncbi.nlm.nih.gov/pmc/articles/PMC14939/>.
4. Wilson CA, Tsuchida MA, Allen GM, Barnhart EL, Applegate KT, Yam PT, et al. Myosin II contributes to cell-scale actin network treadmilling through network disassembly. *Nature*. 2010 05;465(7296):373–377. Available from: <http://dx.doi.org/10.1038/nature08994>.

5. Rauzi M, Lenne PF, Lecuit T. Planar polarized actomyosin contractile flows control epithelial junction remodelling. *Nature*. 2010 Dec;468(7327):1110–1114. Available from: <http://dx.doi.org/10.1038/nature09566>.
6. Munro E, Nance J, Priess JR. Cortical Flows Powered by Asymmetrical Contraction Transport {PAR} Proteins to Establish and Maintain Anterior-Posterior Polarity in the Early *C. elegans* Embryo. *Developmental Cell*. 2004;7(3):413 – 424. Available from: <http://www.sciencedirect.com/science/article/pii/S153458070400276X>.
7. Salbreux G, Charras G, Paluch E. Actin cortex mechanics and cellular morphogenesis. *Trends in Cell Biology*. 2012;22(10):536 – 545. Available from: <http://www.sciencedirect.com/science/article/pii/S0962892412001110>.
8. Murrell M, Oakes PW, Lenz M, Gardel ML. Forcing cells into shape: the mechanics of actomyosin contractility. *Nat Rev Mol Cell Biol*. 2015 08;16(8):486–498. Available from: <http://dx.doi.org/10.1038/nrm4012>.
9. Bendix PM, Koenderink GH, Cuvelier D, Dogic Z, Koeleman BN, Briehar WM, et al. A Quantitative Analysis of Contractility in Active Cytoskeletal Protein Networks. *Biophysical Journal*. 2008;94(8):3126 – 3136. Available from: <http://www.sciencedirect.com/science/article/pii/S0006349508704697>.
10. Janson LW, Kolega J, Taylor DL. Modulation of contraction by gelation/solution in a reconstituted motile model. *The Journal of Cell Biology*. 1991;114(5):1005–1015. Available from: <http://jcb.rupress.org/content/114/5/1005>.
11. Mayer M, Depken M, Bois JS, Julicher F, Grill SW. Anisotropies in cortical tension reveal the physical basis of polarizing cortical flows. *Nature*. 2010 09;467(7315):617–621. Available from: <http://dx.doi.org/10.1038/nature09376>.
12. Bois JS, Jülicher F, Grill SW. Pattern Formation in Active Fluids. *Phys Rev Lett*. 2011 Jan;106:028103. Available from: <http://link.aps.org/doi/10.1103/PhysRevLett.106.028103>.

13. De La Cruz EM, Gardel ML. Actin Mechanics and Fragmentation. *Journal of Biological Chemistry*. 2015 07;290(28):17137–17144. Available from: <http://www.jbc.org/content/290/28/17137>.  
abstractN2-Cellphysiologicalprocessesrequiretheregulationandcoordinationof  
Herewereviewrecentadvancesinunderstandingthemechanicalpropertiesandstability  
lengthscales.  
Wediscusshowforcescaninfluencelocalbiochemicalinteractions,  
resultingintheformationofmechanicallysensitivedynamicsteadystates.  
Understandingtheregulationofsuchforce-activatedchemistriesanddynamicsteady
14. Turlier H, Audoly B, Prost J, Joanny JF. Furrow Constriction in Animal Cell Cytokinesis. *Biophysical Journal*. 2014;106(1):114 – 123. Available from: <http://www.sciencedirect.com/science/article/pii/S0006349513012447>.
15. Salbreux G, Prost J, Joanny JF. Hydrodynamics of Cellular Cortical Flows and the Formation of Contractile Rings. *Phys Rev Lett*. 2009 Jul;103:058102. Available from: <http://link.aps.org/doi/10.1103/PhysRevLett.103.058102>.
16. Keren K, Yam PT, Kinkhabwala A, Mogilner A, Theriot JA. Intracellular fluid flow in rapidly moving cells. *Nat Cell Biol*. 2009 10;11(10):1219–1224. Available from: <http://dx.doi.org/10.1038/ncb1965>.
17. Marchetti MC, Joanny JF, Ramaswamy S, Liverpool TB, Prost J, Rao M, et al. Hydrodynamics of soft active matter. *Rev Mod Phys*. 2013 Jul;85:1143–1189. Available from: <http://link.aps.org/doi/10.1103/RevModPhys.85.1143>.
18. Behrndt M, Salbreux G, Campinho P, Hauschild R, Oswald F, Roensch J, et al. Forces Driving Epithelial Spreading in Zebrafish Gastrulation. *Science*. 2012;338(6104):257–260. Available from: <http://science.sciencemag.org/content/338/6104/257>.
19. Hochmuth RM. Micropipette aspiration of living cells. *Journal of Biomechanics*. 2000;33(1):15 – 22. Available from: <http://www.sciencedirect.com/science/article/pii/S002192909900175X>.

20. Evans E, Yeung A. Apparent viscosity and cortical tension of blood granulocytes determined by micropipet aspiration. *Biophysical Journal*. 1989 07;56(1):151–160. Available from: <http://www.ncbi.nlm.nih.gov/pmc/articles/PMC1280460/>.
21. Bausch AR, Ziemann F, Boulbitch AA, Jacobson K, Sackmann E. Local Measurements of Viscoelastic Parameters of Adherent Cell Surfaces by Magnetic Bead Microrheometry. *Biophysical Journal*. 1998;75(4):2038 – 2049. Available from: <http://www.sciencedirect.com/science/article/pii/S0006349598776465>.
22. De La Cruz EM. How cofilin severs an actin filament. *Biophysical reviews*. 2009 05;1(2):51–59. Available from: <http://www.ncbi.nlm.nih.gov/pmc/articles/PMC2917815/>.
23. Broedersz CP, Depken M, Yao NY, Pollak MR, Weitz DA, MacKintosh FC. Cross-Link-Governed Dynamics of Biopolymer Networks. *Phys Rev Lett*. 2010 Nov;105:238101. Available from: <http://link.aps.org/doi/10.1103/PhysRevLett.105.238101>.
24. Müller KW, Bruinsma RF, Lieleg O, Bausch AR, Wall WA, Levine AJ. Rheology of Semiflexible Bundle Networks with Transient Linkers. *Phys Rev Lett*. 2014 Jun;112:238102. Available from: <http://link.aps.org/doi/10.1103/PhysRevLett.112.238102>.
25. Kim T, Hwang W, Kamm RD. Dynamic Role of Cross-Linking Proteins in Actin Rheology. *Biophysical Journal*. 2011 10;101(7):1597–1603. Available from: <http://www.ncbi.nlm.nih.gov/pmc/articles/PMC3183755/>.
26. Lieleg O, Schmoller KM, Claessens MMAE, Bausch AR. Cytoskeletal Polymer Networks: Viscoelastic Properties are Determined by the Microscopic Interaction Potential of Cross-links. *Biophysical Journal*. 2009 6;96(11):4725–4732. Available from: <http://www.sciencedirect.com/science/article/pii/S0006349509007589>.
27. Lieleg O, Bausch AR. Cross-Linker Unbinding and Self-Similarity in Bundled Cytoskeletal Networks. *Phys Rev Lett*. 2007 Oct;99:158105. Available from: <http://link.aps.org/doi/10.1103/PhysRevLett.99.158105>.

28. Wachsstock DH, Schwarz WH, Pollard TD. Cross-linker dynamics determine the mechanical properties of actin gels. *Biophysical Journal*. 1994;66(3, Part 1):801 – 809. Available from:  
<http://www.sciencedirect.com/science/article/pii/S0006349594808562>.
29. Lieleg O, Claessens MMAE, Luan Y, Bausch AR. Transient Binding and Dissipation in Cross-Linked Actin Networks. *Phys Rev Lett*. 2008 Sep;101:108101. Available from:  
<http://link.aps.org/doi/10.1103/PhysRevLett.101.108101>.
30. Yao NY, Becker DJ, Broedersz CP, Depken M, MacKintosh FC, Pollak MR, et al. Nonlinear Viscoelasticity of Actin Transiently Cross-linked with Mutant alpha-Actinin-4. *Journal of Molecular Biology*. 2011;411(5):1062 – 1071. Available from:  
<http://www.sciencedirect.com/science/article/pii/S0022283611007376>.
31. Liu J, Koenderink GH, Kasza KE, MacKintosh FC, Weitz DA. Visualizing the Strain Field in Semiflexible Polymer Networks: Strain Fluctuations and Nonlinear Rheology of *F*-Actin Gels. *Phys Rev Lett*. 2007 May;98:198304. Available from: <http://link.aps.org/doi/10.1103/PhysRevLett.98.198304>.
32. Robin FB, McFadden WM, Yao B, Munro EM. Single-molecule analysis of cell surface dynamics in *Caenorhabditis elegans* embryos. *Nat Meth*. 2014 06;11(6):677–682. Available from: <http://dx.doi.org/10.1038/nmeth.2928>.
33. Fritzsche M, Lewalle A, Duke T, Kruse K, Charras G. Analysis of turnover dynamics of the submembranous actin cortex. *Molecular Biology of the Cell*. 2013 03;24(6):757–767. Available from:  
<http://www.ncbi.nlm.nih.gov/pmc/articles/PMC3596247/>.
34. Fritzsche M, Erlenkämper C, Moeendarbary E, Charras G, Kruse K. Actin kinetics shapes cortical network structure and mechanics. *Science Advances*. 2016;2(4). Available from:  
<http://advances.sciencemag.org/content/2/4/e1501337>.

35. Carlsson AE. Actin Dynamics: From Nanoscale to Microscale. Annual review of biophysics. 2010 06;39:91–110. Available from:  
<http://www.ncbi.nlm.nih.gov/pmc/articles/PMC2967719/>.
36. Lai FP, Szczodrak M, Block J, Faix J, Breitsprecher D, Mannherz HG, et al. Arp2/3 complex interactions and actin network turnover in lamellipodia. The EMBO Journal. 2008 04;27(7):982–992. Available from:  
<http://www.ncbi.nlm.nih.gov/pmc/articles/PMC2265112/>.
37. Van Goor D, Hyland C, Schaefer AW, Forscher P. The Role of Actin Turnover in Retrograde Actin Network Flow in Neuronal Growth Cones. PLoS ONE. 2012;7(2):e30959. Available from:  
<http://www.ncbi.nlm.nih.gov/pmc/articles/PMC3281045/>.
38. Lenz M, Gardel ML, Dinner AR. Requirements for contractility in disordered cytoskeletal bundles. New Journal of Physics. 2012;14(3):033037. Available from:  
<http://stacks.iop.org/1367-2630/14/i=3/a=033037>.
39. Lenz M. Geometrical Origins of Contractility in Disordered Actomyosin Networks. Phys Rev X. 2014 Oct;4:041002. Available from:  
<http://link.aps.org/doi/10.1103/PhysRevX.4.041002>.
40. Murrell MP, Gardel ML. F-actin buckling coordinates contractility and severing in a biomimetic actomyosin cortex. Proceedings of the National Academy of Sciences. 2012;109(51):20820–20825. Available from:  
<http://www.pnas.org/content/109/51/20820.abstract>.
41. Alvarado J, Sheinman M, Sharma A, MacKintosh FC, Koenderink GH. Molecular motors robustly drive active gels to a critically connected state. Nat Phys. 2013 09;9(9):591–597. Available from: <http://dx.doi.org/10.1038/nphys2715>.
42. Murrell M, Gardel ML. Actomyosin sliding is attenuated in contractile biomimetic cortices. Molecular Biology of the Cell. 2014;25(12):1845–1853. Available from:  
<http://www.molbiolcell.org/content/25/12/1845.abstract>.

43. Ennomani H, Letort G, Guérin C, Martiel JL, Cao W, Nédélec F, et al. Architecture and Connectivity Govern Actin Network Contractility. *Current Biology*. 2016;26(5):616 – 626. Available from: <http://www.sciencedirect.com/science/article/pii/S0960982216000543>.
44. Reymann AC, Boujemaa-Paterski R, Martiel JL, Guérin C, Cao W, Chin HF, et al. Actin Network Architecture Can Determine Myosin Motor Activity. *Science*. 2012;336(6086):1310–1314. Available from: <http://science.sciencemag.org/content/336/6086/1310>.
45. Nedelec FJ, Surrey T, Maggs AC, Leibler S. Self-organization of microtubules and motors. *Nature*. 1997 09;389(6648):305–308. Available from: <http://dx.doi.org/10.1038/38532>.
46. Surrey T, Nédélec F, Leibler S, Karsenti E. Physical Properties Determining Self-Organization of Motors and Microtubules. *Science*. 2001;292(5519):1167–1171. Available from: <http://science.sciencemag.org/content/292/5519/1167>.
47. Hiraiwa T, Salbreux G. Role of turn-over in active stress generation in a filament network. *ArXiv e-prints*. 2015 Jul;
48. Mak M, Zaman MH, Kamm RD, Kim T. Interplay of active processes modulates tension and drives phase transition in self-renewing, motor-driven cytoskeletal networks. *Nat Commun*. 2016 01;7. Available from: <http://dx.doi.org/10.1038/ncomms10323>.
49. Zumdieck A, Kruse K, Bringmann H, Hyman AA, Jülicher F. Stress Generation and Filament Turnover during Actin Ring Constriction. *PLoS ONE*. 2007 08;2(8):e696. Available from: <http://dx.plos.org/10.1371/journal.pone.0000696>.
50. Dierkes K, Sumi A, Solon J, Salbreux G. Spontaneous Oscillations of Elastic Contractile Materials with Turnover. *Phys Rev Lett*. 2014 Oct;113:148102. Available from: <http://link.aps.org/doi/10.1103/PhysRevLett.113.148102>.

51. Vanossi A, Manini N, Urbakh M, Zapperi S, Tosatti E. *Colloquium* : Modeling friction: From nanoscale to mesoscale. *Rev Mod Phys*. 2013 Apr;85:529–552. Available from: <http://link.aps.org/doi/10.1103/RevModPhys.85.529>.
52. Spruijt E, Sprakel J, Lemmers M, Stuart MAC, van der Gucht J. Relaxation Dynamics at Different Time Scales in Electrostatic Complexes: Time-Salt Superposition. *Phys Rev Lett*. 2010 Nov;105:208301. Available from: <http://link.aps.org/doi/10.1103/PhysRevLett.105.208301>.
53. Filippov AE, Klafter J, Urbakh M. Friction through Dynamical Formation and Rupture of Molecular Bonds. *Phys Rev Lett*. 2004 Mar;92:135503. Available from: <http://link.aps.org/doi/10.1103/PhysRevLett.92.135503>.
54. Banerjee S, Marchetti MC, Müller-Nedebock K. Motor-driven dynamics of cytoskeletal filaments in motility assays. *Phys Rev E*. 2011 Jul;84:011914. Available from: <http://link.aps.org/doi/10.1103/PhysRevE.84.011914>.
55. Chugh P, Clark AG, Smith MB, Cassani DAD, Charras G, Salbreux G, et al. Nanoscale Organization of the Actomyosin Cortex during the Cell Cycle. *Biophysical Journal*. 2016 2016/07/18;110(3):198a. Available from: <http://dx.doi.org/10.1016/j.bpj.2015.11.1105>.
56. Sanchez T, Chen DTN, DeCamp SJ, Heymann M, Dogic Z. Spontaneous motion in hierarchically assembled active matter. *Nature*. 2012 11;491(7424):431–434. Available from: <http://dx.doi.org/10.1038/nature11591>.
57. Broedersz CP, Storm C, MacKintosh FC. Effective-medium approach for stiff polymer networks with flexible cross-links. *Phys Rev E*. 2009 Jun;79:061914. Available from: <http://link.aps.org/doi/10.1103/PhysRevE.79.061914>.
58. Head DA, Levine AJ, MacKintosh FC. Deformation of Cross-Linked Semiflexible Polymer Networks. *Phys Rev Lett*. 2003 Sep;91:108102. Available from: <http://link.aps.org/doi/10.1103/PhysRevLett.91.108102>.
59. Wilhelm J, Frey E. Elasticity of Stiff Polymer Networks. *Phys Rev Lett*. 2003 Sep;91:108103. Available from: <http://link.aps.org/doi/10.1103/PhysRevLett.91.108103>.

60. Ward A, Hilitski F, Schwenger W, Welch D, Lau AWC, Vitelli V, et al. Solid friction between soft filaments. *Nat Mater.* 2015 03;advance online publication:–. Available from: <http://dx.doi.org/10.1038/nmat4222>.
61. Chandran PL, Mofrad MRK. Averaged implicit hydrodynamic model of semiflexible filaments. *Phys Rev E.* 2010 Mar;81:031920. Available from: <http://link.aps.org/doi/10.1103/PhysRevE.81.031920>.
62. Unterberger MJ, Holzapfel GA. Advances in the mechanical modeling of filamentous actin and its cross-linked networks on multiple scales. *Biomechanics and Modeling in Mechanobiology.* 2014;13(6):1155–1174. Available from: <http://dx.doi.org/10.1007/s10237-014-0578-4>.
63. McCrum NG, Buckley CP, Bucknall CB. *Principles of Polymer Engineering.* Oxford science publications. Oxford University Press; 1997. Available from: <https://books.google.com/books?id=EiqWQgAACAAJ>.
64. Kim T, Gardel ML, Munro E. Determinants of Fluidlike Behavior and Effective Viscosity in Cross-Linked Actin Networks. *Biophysical Journal.* 2014;106(3):526 – 534. Available from: <http://www.sciencedirect.com/science/article/pii/S0006349513058487>.
65. Koenderink GH, Dogic Z, Nakamura F, Bendix PM, MacKintosh FC, Hartwig JH, et al. An active biopolymer network controlled by molecular motors. *Proceedings of the National Academy of Sciences of the United States of America.* 2009 09;106(36):15192–15197. Available from: <http://www.ncbi.nlm.nih.gov/pmc/articles/PMC2741227/>.
66. Gorfinkiel N, Blanchard GB. Dynamics of actomyosin contractile activity during epithelial morphogenesis. *Current Opinion in Cell Biology.* 2011;23(5):531 – 539. Cell-to-cell contact and extracellular matrix. Available from: <http://www.sciencedirect.com/science/article/pii/S0955067411000834>.
67. Theriot JA, Mitchison TJ. Actin microfilament dynamics in locomoting cells. *Nature.* 1991 Jul;352(6331):126–131. Available from: <http://dx.doi.org/10.1038/352126a0>.

68. Murthy K, Wadsworth P. Myosin-II-Dependent Localization and Dynamics of F-Actin during Cytokinesis. *Current Biology*. 2016 2016/12/15;15(8):724–731. Available from: <http://dx.doi.org/10.1016/j.cub.2005.02.055>.
69. Watanabe N, Mitchison TJ. Single-Molecule Speckle Analysis of Actin Filament Turnover in Lamellipodia. *Science*. 2002;295(5557):1083–1086. Available from: <http://science.sciencemag.org/content/295/5557/1083>.
70. Guha M, Zhou M, Wang YL. Cortical Actin Turnover during Cytokinesis Requires Myosin II. *Current Biology*. 2016 2016/12/15;15(8):732–736. Available from: <http://dx.doi.org/10.1016/j.cub.2005.03.042>.
71. Fritzsche M, Lewalle A, Duke T, Kruse K, Charras G. Analysis of turnover dynamics of the submembranous actin cortex. *Molecular Biology of the Cell*. 2013;24(6):757–767. Available from: <http://www.molbiolcell.org/content/24/6/757.abstract>.

## S1 Appendix

### A.1 Simulation and Analysis Code Available Online

All of the simulation and analysis code for generating the figures in this paper is available online. To find the source code please visit our Github repository at <https://github.com/wmcfadden/activnet>

### A.2 Steady-state Approximation of Effective Viscosity

We begin with a calculation of a strain rate estimate of the effective viscosity for a network described by our model in the limit of highly rigid filaments. We carry this out by assuming we have applied a constant stress along a transect of the network. With moderate stresses, we assume the network reaches a steady state affine creep. In this situation, we would find that the stress in the network exactly balances the sum of the drag-like forces from cross-link slip. So for any transect of length  $D$ , we have a force balance equation.

$$\sigma = \frac{1}{D} \sum_{\text{filaments}} \sum_{\text{crosslinks}} \xi \cdot (\mathbf{v}_i(\mathbf{x}) - \mathbf{v}_j(\mathbf{x})) \quad (15)$$

where  $\mathbf{v}_i(\mathbf{x}) - \mathbf{v}_j(\mathbf{x})$  is the difference between the velocity of a filament,  $i$ , and the velocity of the filament,  $j$ , to which it is attached at the cross-link location,  $\mathbf{x}$ . We can convert the sum over cross-links to an integral over the length using the average density of cross-links,  $1/l_c$  and invoking the assumption of (linear order) affine strain rate,  $\mathbf{v}_i(\mathbf{x}) - \mathbf{v}_j(\mathbf{x}) = \dot{\gamma}x$ . This results in

$$\begin{aligned} \sigma &= \frac{1}{D} \sum_{\text{filaments}} \int_0^L \xi \cdot (\mathbf{v}_i(\mathbf{s}) - \mathbf{v}_j(\mathbf{s})) \frac{ds \cos \theta}{l_c} \\ &= \sum_{\text{filaments}} \frac{\xi \dot{\gamma} L}{l_c} \cos \theta \cdot \left(x_l + \frac{L}{2} \cos \theta\right) \end{aligned} \quad (16)$$

Here we have introduced the variables  $x_l$ , and  $\theta$  to describe the leftmost endpoint and the angular orientation of a given filament respectively. Next, to perform the sum over all filaments we convert this to an integral over all orientations and endpoints that intersect our line of stress. We assume for simplicity that filament stretch and filament alignment are negligible in this low strain approximation. Therefore, the max distance for the leftmost endpoint is the length of a filament,  $L$ , and the maximum angle as a function of endpoint is  $\arccos(x_l/L)$ . The linear density of endpoints is the constant  $D/l_c L$  so our integrals can be rewritten as this density over  $x_l$  and  $\theta$  between our maximum and minimum allowed bounds.

$$\sigma = \frac{1}{D} \int_0^L dx_l \int_{-\arccos(\frac{x_l}{L})}^{\arccos(\frac{x_l}{L})} \pi d\theta \frac{\xi \dot{\gamma} L}{l_c} \cdot \frac{D}{L l_c} \cdot \left(x_l \cos \theta + \frac{L}{2} \cos^2 \theta\right) \quad (17)$$

Carrying out the integrals and correcting for dangling filament ends leaves us with a relation between stress and strain rate.

$$\sigma = 4\pi \left(\frac{L}{l_c} - 1\right)^2 \xi \dot{\gamma} \quad (18)$$

We recognize the constant of proportionality between stress and strain rate as a viscosity (in 2 dimensions). Therefore, our approximation for the effective viscosity,  $\eta_c$ ,

at steady state creep in this low strain limit is

$$\sigma = 4\pi \left( \frac{L}{l_c} - 1 \right)^2 \xi \quad (19)$$

### A.3 Critical filament lifetime for steady state filament extension

We seek to determine a critical filament lifetime,  $\tau_{crit}$ , below which the density of filaments approaches a stable steady state under constant extensional strain. To this end, let  $\rho$  be the filament density (i.e. number of filaments per unit area). We consider a simple coarse grained model for how  $\rho$  changes as a function of filament assembly  $k_{ass}$ , filament disassembly  $k_{diss}$ ,  $\rho$  and strain thinning  $\dot{\gamma}\rho$ . Using  $\rho_0 = \frac{k_{ass}}{k_{diss}}$ ,  $\tau_r = \frac{1}{k_{diss}}$ , and  $\dot{\gamma} = \frac{\sigma}{\eta_c}$ .

$$\frac{d\rho}{dt} = \frac{1}{\tau_r} \left( \rho_0 - \rho - \frac{\sigma\tau_r}{\eta_c(\rho)}\rho \right) \quad (20)$$

where  $\eta_c = \eta_c(\rho)$  on the right hand side reflects the dependence of effective viscosity on network density. The strength of this dependence determines whether there exists a stable steady state, representing continuous flow. Using  $\eta_c(\rho) \sim \xi \left( \frac{L}{l_c(\rho)} - 1 \right)^2$  from above (ignoring the numerical prefactor) and  $\rho \sim \frac{2}{Ll_c(\rho)}$ , we obtain:

$$\frac{d\rho}{dt} = \frac{1}{\tau_r} \left( \rho_0 - \rho - \frac{\sigma\tau_r}{\xi(\rho L^2/2 - 1)^2}\rho \right) \quad (21)$$

Fig. A.1 sketches the positive ( $\rho_0$ ) and negative ( $\rho + \frac{\sigma\tau_r}{\eta_c(\rho)}\rho$ ) contributions to the right hand side of Equation 6 for different values of  $\tau_r$ . For sufficiently large  $\tau_r$ , there is no stable state, i.e. strain thinning will occur. However, as  $\tau_r$  decreases below a critical value  $\tau_{crit}$ , a stable steady state appears. Note that when  $\tau_r = \tau_{crit}$ ,  $\rho + \frac{\sigma\tau_r}{\eta_c(\rho)}\rho$  passes through a minimum value  $\rho_0$  at  $\rho = \rho^*$ . Accordingly, to determine  $\tau_{crit}$ , we solve:

$$0 = \frac{d}{d\rho} \left( \rho + \frac{\sigma\tau_r}{\eta_c(\rho)}\rho \right) = 1 - \frac{\sigma\tau_r}{\xi(\rho L^2/2 - 1)^3} \quad (22)$$

From this, with some algebra, we infer that

$$\rho^* = \frac{2}{L^2} \left( 1 + \left( \frac{\sigma\tau_r}{\xi} \right)^{1/3} \right) \quad (23)$$

and

$$\frac{\sigma\tau_r}{\eta_c(\rho^*)} = \left(\frac{\sigma\tau_r}{\xi}\right)^{1/3} \tag{24}$$

We seek a value for  $\tau_r = \tau_{crit}$  at which

$$\rho^* + \frac{\sigma\tau_{crit}}{\eta_c(\rho^*)}\rho^* = \rho_0 \tag{25}$$

Substituting from above, and using  $\rho_0 = \frac{2}{Ll_c}$ , we have:

$$\frac{2}{L^2} \left(1 + \left(\frac{\sigma\tau_{crit}}{\xi}\right)^{1/3}\right) \left(1 + \left(\frac{\sigma\tau_{crit}}{\xi}\right)^{1/3}\right) = \frac{2}{Ll_c} \tag{26}$$

Finally, rearranging terms, we obtain

$$\tau_{crit} = \frac{\xi}{\sigma} \left(\sqrt{\frac{L}{l_c}} - 1\right)^3 \tag{27}$$

**Table 2.** Parameter values sampled for individual figures

Parameter	Figure 3	Figure 4	Figure S3a,b	Figure S3c,d	Figure 7	Figure 9
$L$	1, 3, 5, 7, 10	3	3, 5	3, 5	5	3, 5, 8
$l_c$	0.2, 0.3, 0.5, 0.8	0.3, 0.5	0.3	0.15, 0.2, 0.3, 0.4	0.2, 0.3	0.15, 0.2, 0.3, 0.4
$\mu_e/\mu_c$	100	100	3 – 300	100	100	100
$\mu_c$	0.01	0.01	0.01 – 0.3	0.001 – 0.03	0.01	0.01
$\xi$	0.1, 1	0.05, 0.1, 1	0.01, 0.1, 1	0.1, 1	0.1, 1, 3.3	0.1, 1
$v$			0.1, 0.3, 1	0.1, 1	0.1, 1, 3	0.1
$\phi$			0.25	0.5	0.25, 0.75	0.25
$\tau_r$		$0.1 - 10^4$			$0.01 - 10^3$	$0.01 - 10^3$
$\sigma$	$0.0002 - 0.01$	$0.00003 - 0.005$				

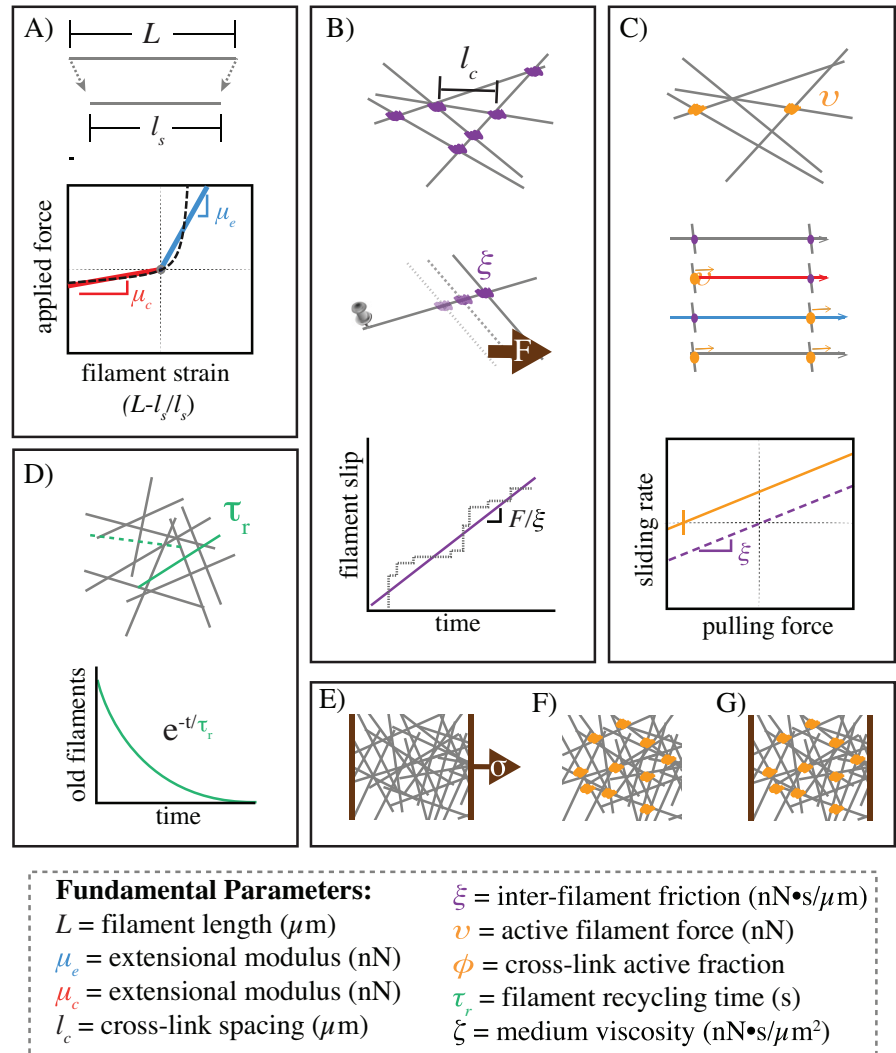


**Fig 1.** Schematic overview of modeling framework and assumptions. **A)** Filaments are oriented linear springs that are stiffer in extension than in compression. **B)** Cross-linking occurs at all filament crossings; we represent cross link resistance as an effective drag, proportional to the relative velocity of the overlapping filaments. **C)** We represent motor activity as a linear force-velocity relationship with a fixed force at zero velocity directed towards a filament's (-) end. We implement spatial heterogeneity by imposing motor activity at a fixed fraction of filament crossover points, resulting in variation in the magnitudes of compressive vs extensile vs translational forces along individual filament segments. **D)** Whole filaments disappear at a constant rate; new filaments appear with random positions and orientations at the constant rate per unit area, such that entire network refreshes on a characteristic timescale  $\tau_r$ . **e-g)** Three different simulation scenarios: **E)** Passive response to uniaxial stress, **F)** Free contraction of an active network and **G)** Isometric contraction against a fixed boundary.

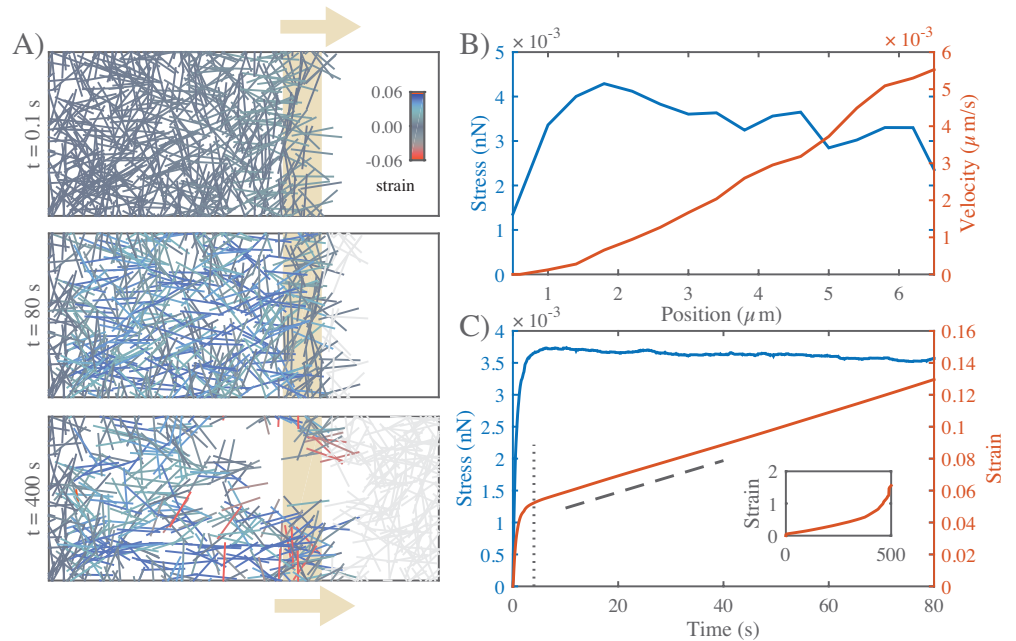


**Fig 2.** Networks with passive cross-links and no filament turnover undergo three stages of deformation in response to an extensional stress. **A)** Three successive time points from a simulation of a  $4 \times 6.6 \mu\text{m}$  network deforming under an applied stress of  $0.005 \text{ nN}/\mu\text{m}$ . Stress (tan arrows) is applied to filaments in the region indicated by the tan bar. In this and all subsequent figures, filaments are color-coded with respect to state of strain (blue = tension, red = compression). Network parameters:  $L = 1 \mu\text{m}$ ,  $l_c = 0.3 \mu\text{m}$ ,  $\xi = 100 \text{ nN} \cdot \text{s}/\mu\text{m}$ . **B)** Mean filament stress and velocity profiles for the network in (a) at  $t=88\text{s}$ . Note that the stress is nearly constant and the velocity is nearly linear as predicted for a viscous fluid under extension. **C)** Plots of the mean stress and strain vs time for the simulation in (a), illustrating the three stages of deformation: (i) A fast initial deformation accompanies rapid buildup of internal network stress; (ii) after a characteristic time  $\tau_c$  (indicated by vertical dotted line) the network deforms at a constant rate, i.e. with a constant effective viscosity,  $\eta_c$ , given by the slope of the dashed line; (iii) at long times, the network undergoes strain thinning and tearing (see inset)

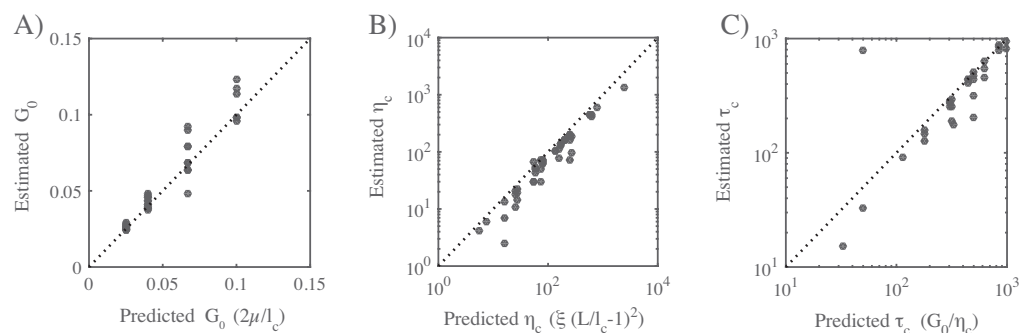


**Fig 3.** Network architecture sets the rate and timescales of deformation. **(a-c)** Comparison of predicted and simulated values for: **A)** the bulk elastic modulus  $G_0$ , **B)** the effective viscosity  $\eta_c$  and **C)** the timescale for transition from viscoelastic to viscous behavior  $\tau_c$ , given by the ratio of the bulk elastic modulus  $G_0$  to effective viscosity,  $\eta_c$ . Dotted lines indicates the relationships predicted by theory.

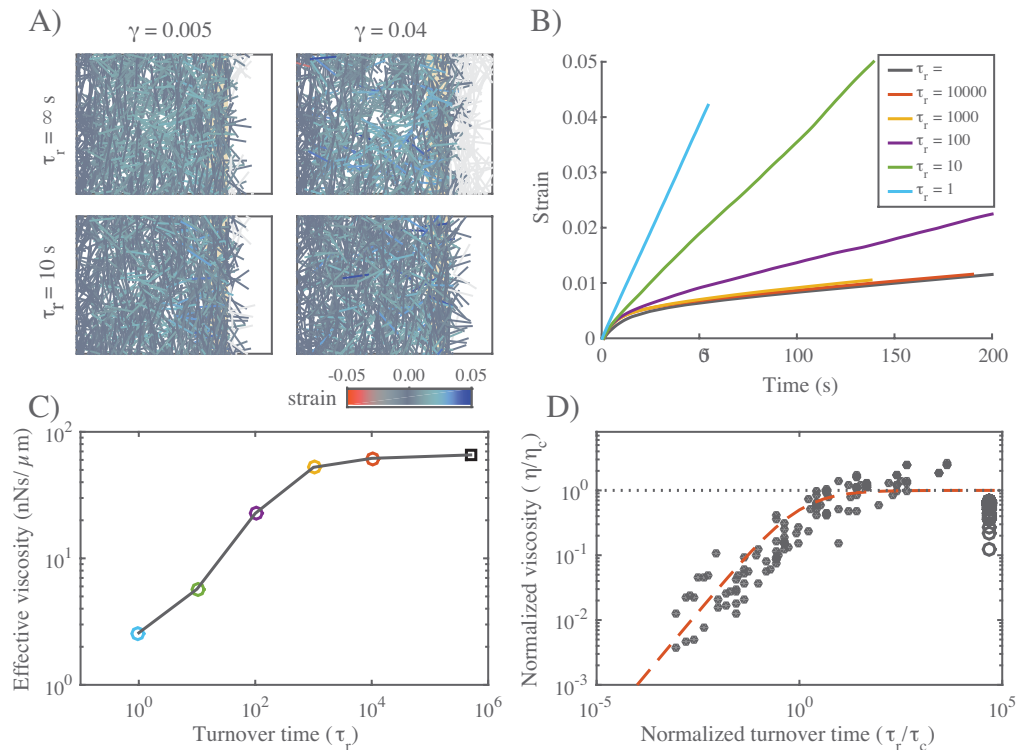


**Fig 4.** Filament recycling defines two regimes of effectively viscous flow. **A)** Comparison of  $20 \times 12 \mu\text{m}$  networks under  $0.001 \text{ nN}/\mu\text{m}$  extensional stress without (top) and with (bottom) filament turnover. Both images are taken when the networks had reached a net strain of 0.04. For clarity, filaments that leave the domain of applied stress are greyed out. **B)** Plots of strain vs time for identical networks with different rates of filament turnover. Network parameters:  $L = 5 \mu\text{m}$ ,  $l_c = 0.5 \mu\text{m}$ ,  $\xi = 10 \text{ nN} \cdot \text{s}/\mu\text{m}$ . **C)** Plot of effective viscosity vs turnover time derived from the simulations shown in panel b. Square dot is the  $\tau_r = \infty$  condition. **D)** Plot of normalized effective viscosity ( $\eta/\eta_c$ ) vs normalized turnover time ( $\tau_r/\tau_c$ ) for a large range of network parameters and turnover times. For  $\tau_r \ll \tau_c$ , the viscosity of the network becomes dependent on recycling time. Red dashed line indicates the approximation given in equation 11 for  $m = 3/4$ .

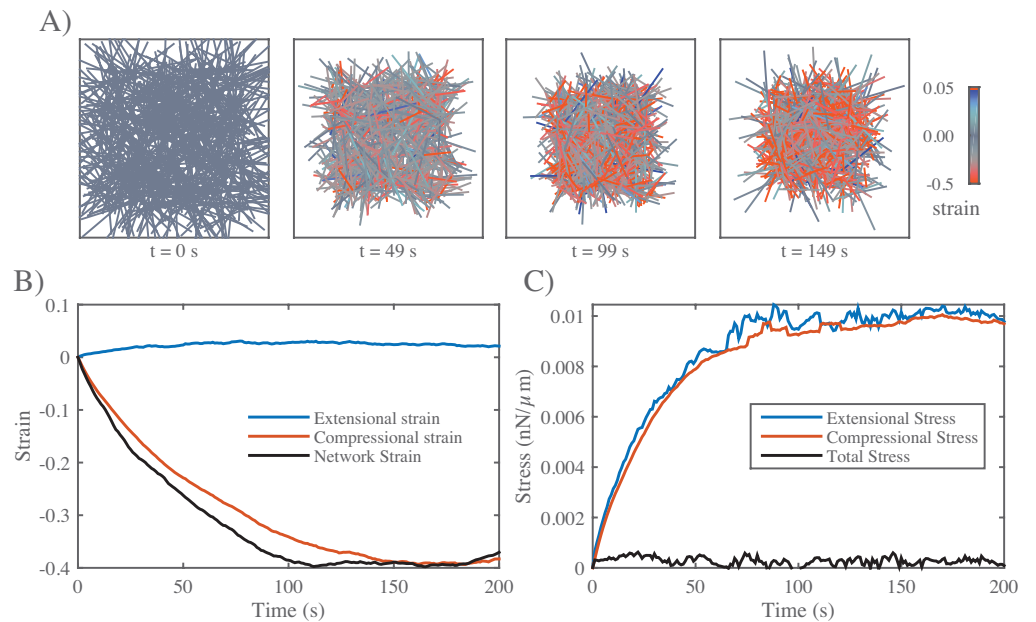


**Fig 5.** In the absence of filament turnover, active networks with free boundaries contract and then stall against passive resistance to network compression. **A)** Simulation of an active network with free boundaries. Colors represent strain on individual filaments as in previous figures. Note the buildup of compressive strain as contraction approaches stall between 100 s and 150 s. Network parameters:  $L = 5 \mu m$ ,  $l_c = 0.3 \mu m$ ,  $\xi = 1 nN \cdot s/\mu m$ ,  $v = 0.1 nN$ . **B)** Plots showing time evolution of total network strain (black) and the average extensional (blue) or compressive (red) strain on individual filaments. **C)** Plots showing time evolution of total (black) extensional (blue) or compressive (red) stress. Note that extensional and compressive stress remain balanced as compressive resistance builds during network contraction.

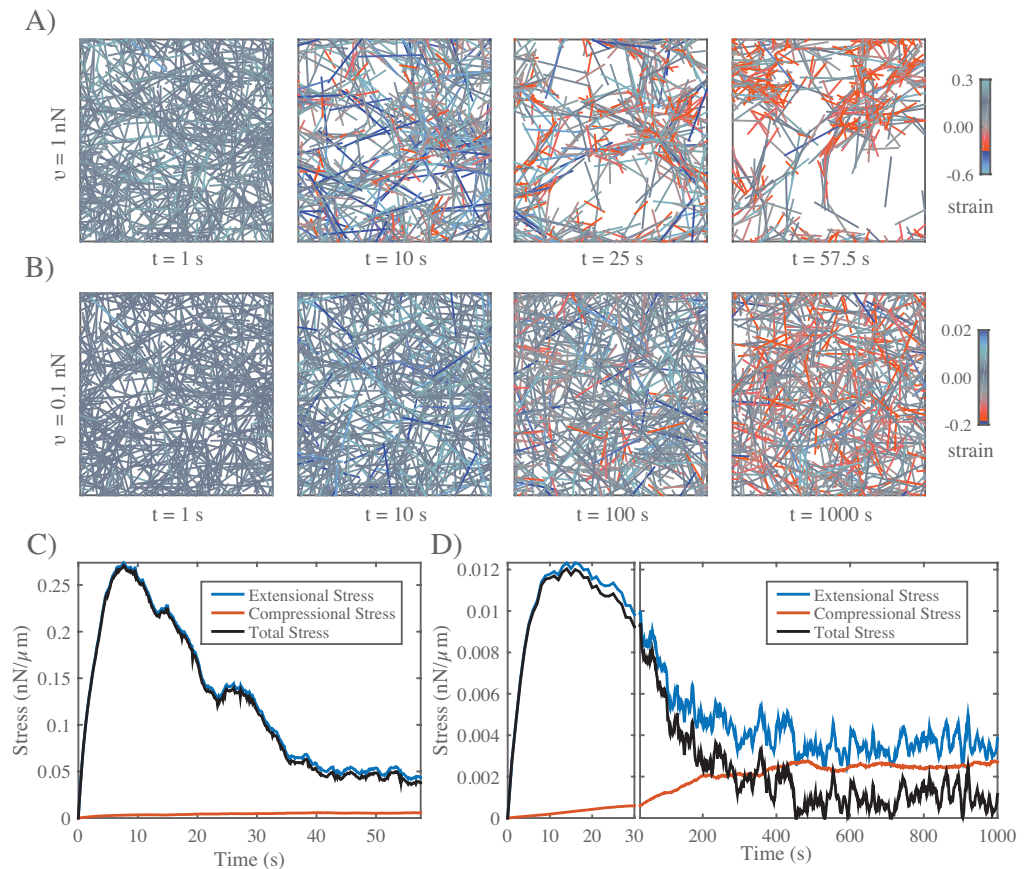


**Fig 6.** In the absence of filament turnover, active networks cannot sustain continuous stress against a fixed boundary. **A)** Simulation of an active network with fixed boundaries. Rearrangement of network filaments by motor activity leads to rapid loss of network connectivity. Network parameters:  $L = 5 \mu\text{m}$ ,  $l_c = 0.3 \mu\text{m}$ ,  $\xi = 1 \text{ nN} \cdot \text{s}/\mu\text{m}$ ,  $v = 1 \text{ nN}$ . **B)** Simulation of the same network, with the same parameter values, except with ten-fold lower motor activity  $v = 0.1 \text{ nN}$ . In this case, connectivity is preserved, but there is a progressive buildup of compressive strain on individual filaments. **C)** Plots of total network stress and the average extensional (blue) and compressive (red) stress on individual filaments for the simulation shown in (a). Rapid buildup of extensional stress allows the network transiently to exert force on its boundary, but this force is rapidly dissipated as network connectivity breaks down. **D)** Plots of total network stress and the average extensional (blue) and compressive (red) stress on individual filaments for the simulation shown in (b). Rapid buildup of extensional stress allows the network transiently to exert force on its boundary, but this force is dissipated at longer times as decreasing extensional stress and increasing compressive stress approach balance. Note the different time scales used for plots and subplots in **C)** and **D)** to emphasize the similar timescales for force buildup, but very different timescales for force dissipation.

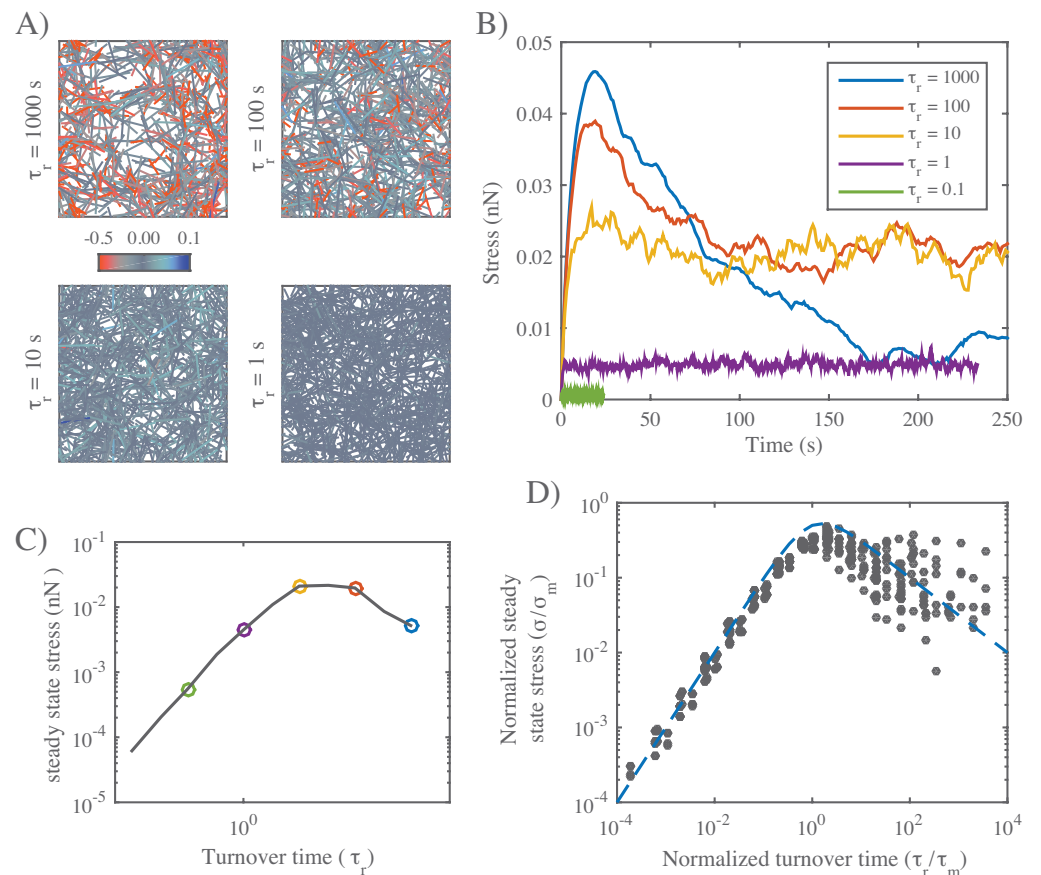


**Fig 7.** Filament turnover allows active networks to exert sustained stress on a fixed boundary. **A)** Snapshots from simulations of active networks with fixed boundaries and different rates of filament turnover. All other parameter values are the same as in Fig. 6A. Note the significant buildup of compressive strain and significant remodeling for longer, but not shorter, turnover times. **B)** Plots of net stress exerted by the network on its boundaries for different recycling times; for long-lived filaments, stress is built rapidly, but then dissipates. Decreasing filament lifetimes reduces stress dissipation by replacing compressed with uncompressed filaments, allowing higher levels of steady state stress; for very short lifetimes, stress is reduced, because individual filaments do not have time to build stress before turning over. **C)** Plots of  $\approx$ steady state stress estimated from the simulations in **B)** vs turnover time. **D)** Plot of normalized steady state stress vs normalized recycling time for a wide range of network parameters and turnover times. Steady state stress is normalized by the predicted maximum stress  $\sigma_m$  achieved in the absence of filament turnover. Turnover time is normalized by the predicted time to achieve maximum stress  $\tau_m$ , in the absence of filament turnover. Predictions for  $\sigma_m$  and  $\tau_m$  were obtained from the phenomenological scaling relations shown in (Fig. C,D). Dashed blue line indicates the approximation given in equation 12 for  $n = 1$ .

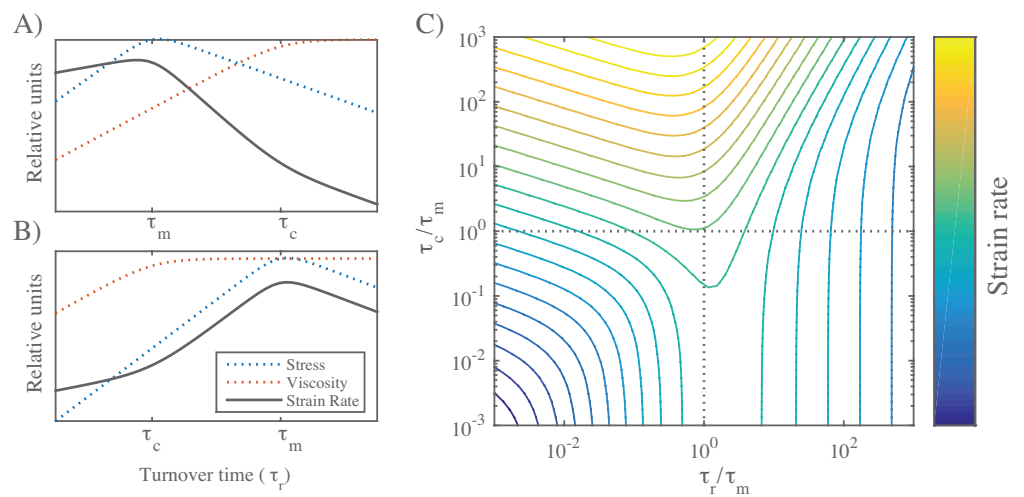


**Fig 8.** Filament recycling tunes the magnitudes of both effective viscosity and steady state stress. **A)** Dependence of steady state stress, effective viscosity, and resulting strain rate on recycling time  $\tau_r$  under the condition  $\tau_m < \tau_c$ . **B)** Same as a) but for  $\tau_c < \tau_m$ . **C)** State space of flow rate dependence relative to the two relaxation timescales,  $\tau_r$  and  $\tau_c$  normalized by the stress buildup timescale,  $\tau_m$ .

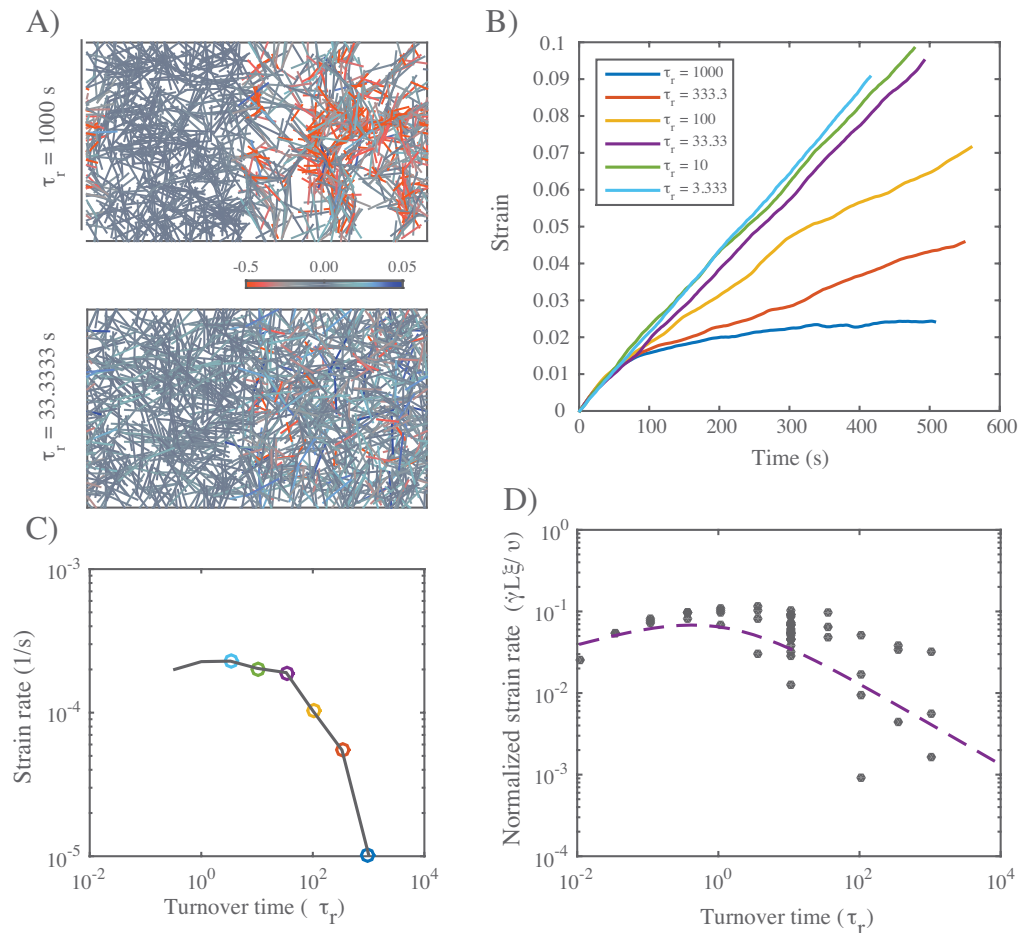


**Fig 9.** Filament recycling allows sustained flows in networks with non-isotropic activity. **A)** Example simulations of non-isotropic networks with long ( $\tau_r = 1000$ ) and short ( $\tau_r = 33$ ) recycling timescales. In these networks the left half of the network is passive while the right half is active. Network parameters are same as in Figs 6 and 7. Importantly, in all simulations  $\tau_m < \tau_c$ . **B)** Graph of strain for identical networks with varying recycling timescales. With long recycling times, the network stalls; reducing the recycling timescale allows the network to persist in its deformation. However, for the shortest recycling timescales, the steady state strain begins to slowly return to 0 net motion. Measurements are based on the passive side of the network. **C)** Steady state strain rates for the networks in (b). **D)** Graph of network's long-term strain rate as a function of recycling timescale. Dashed line is form of dependence predicted by the theoretical arguments shown in Fig. 8.

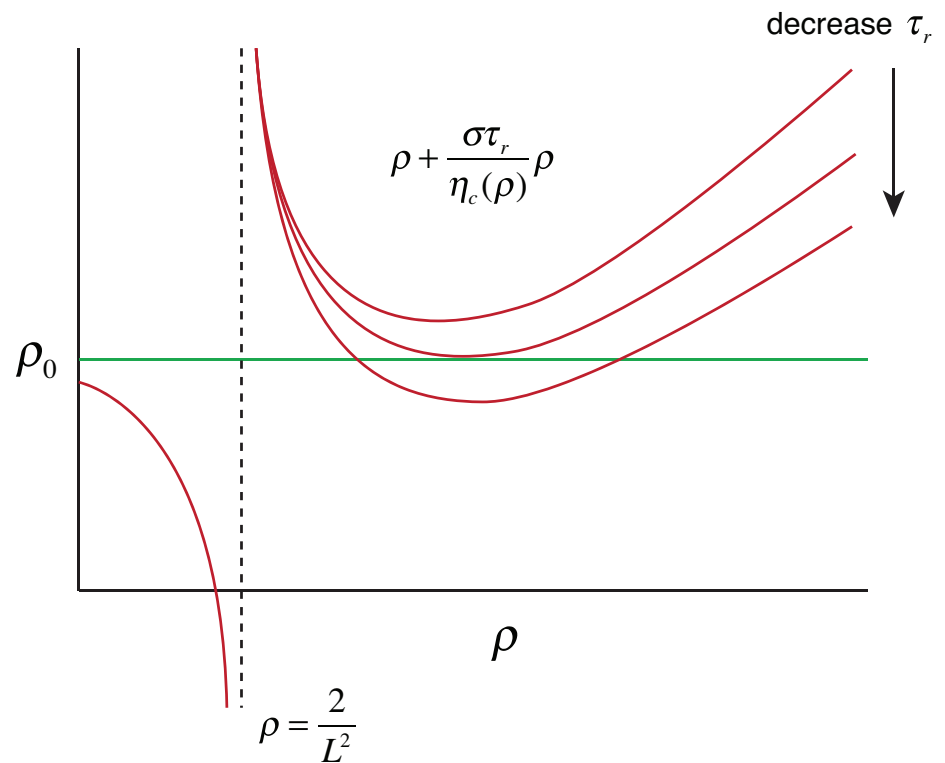
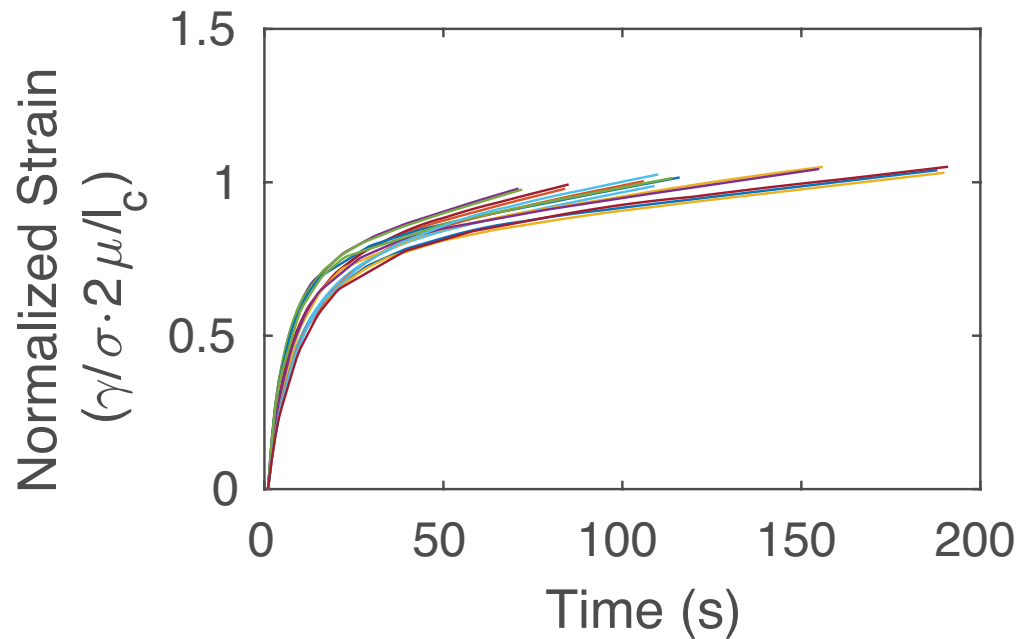
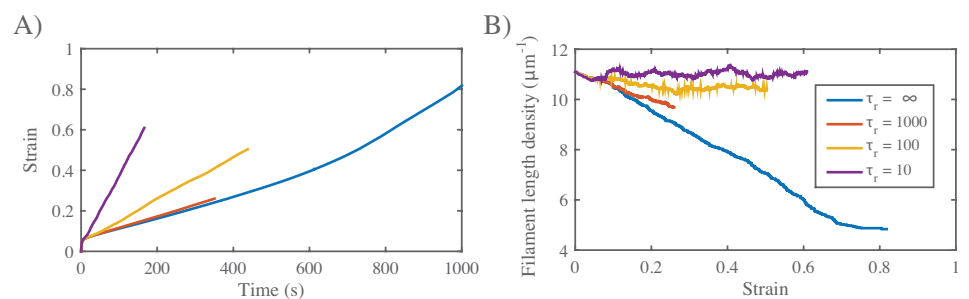


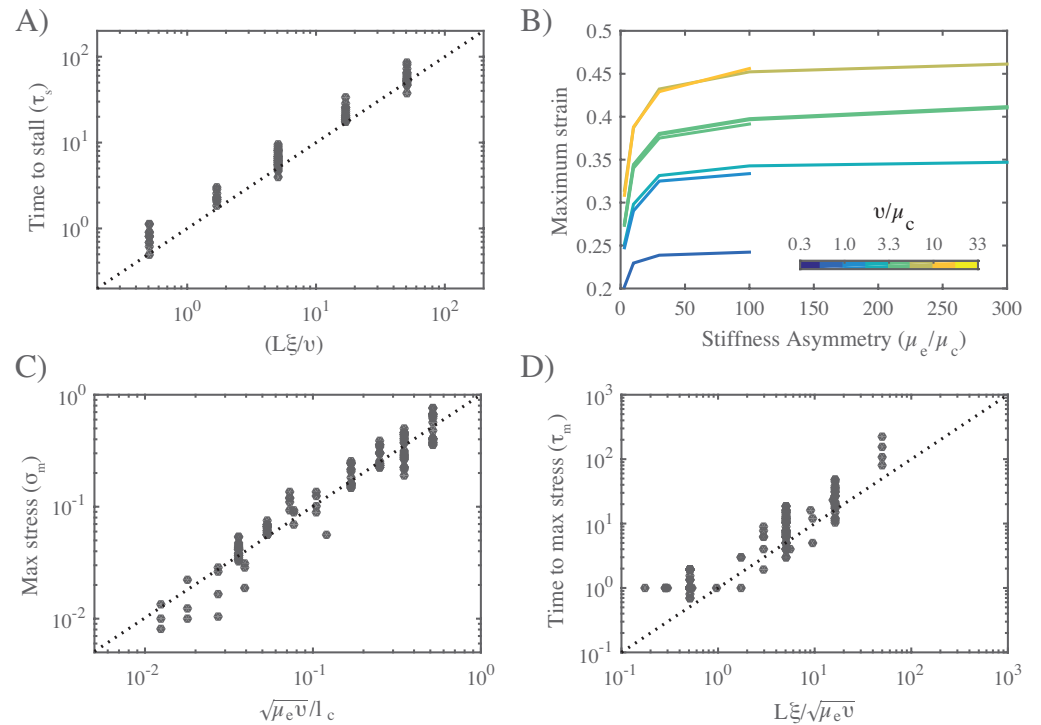
**Fig. A.1** Flux balance analysis of network density. Qualitative plots of  $\rho + \frac{\sigma\tau_r}{\eta_c(\rho)}\rho$  (red curves) vs  $\rho_0$  (green line) for different values of  $\tau_r$ . For sufficiently large  $\tau_r$ , there are no crossings. For  $\tau_r < \tau_{crit}$ , there are two crossings: The rightmost crossing represents a stable steady state.



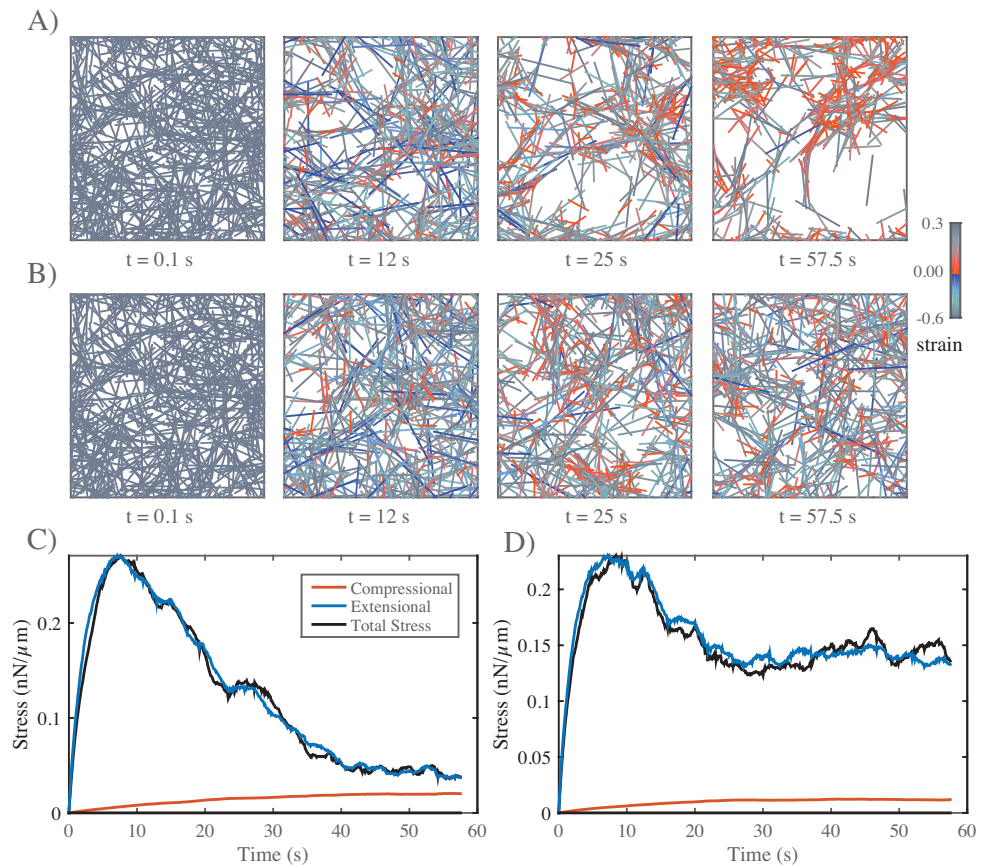
**S1 Fig.** Fast viscoelastic response to extensional stress. Plots of normalized strain vs time during the elastic phase of deformation in passive networks under extensional stress. Measured strain is normalized by the equilibrium strain predicted for a network of elastic filaments without crosslink slip  $\gamma_{eq} = \sigma/G_0 = \sigma/(2\mu/l_c)$ .



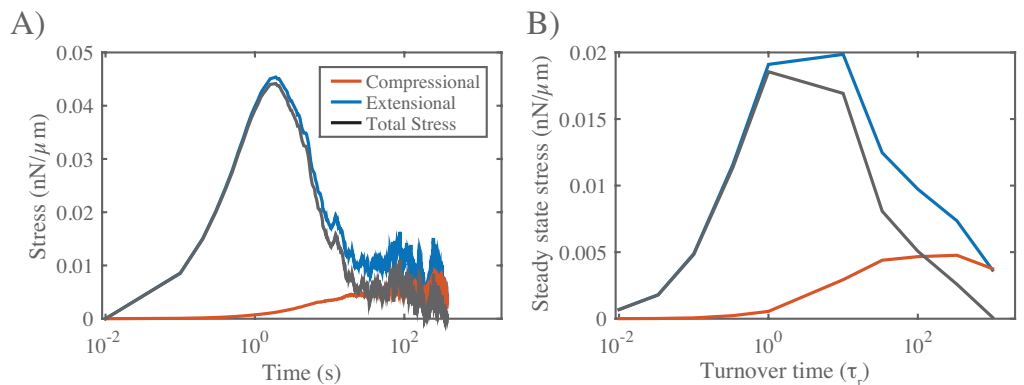
**S2 Fig.** Filament turnover rescues strain thinning. **A)** Plots of strain vs time for different turnover times (see inset in (B)). Note the increase in strain rates with decreasing turnover time. **B)** Plots of filament density vs strain for different turnover times  $\tau_r$ . For intermediate  $\tau_r$ , simulations predict progressive strain thinning, but at a lower rate than in the complete absence of recycling. For higher  $\tau_r$ , densities approach steady state values at longer times.



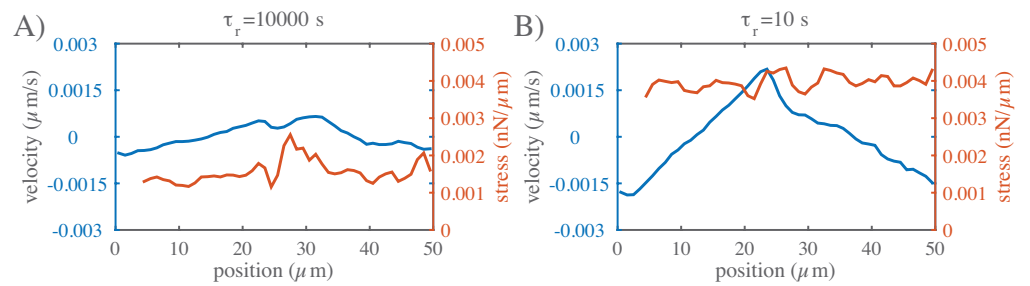
**S3 Fig.** Mechanical properties of active networks. **A)** Time for freely contracting networks to reach maximum strain,  $\tau_s$ , scales with  $L\xi/v$ . **B)** Free contraction requires asymmetric filament compliance, and total network strain increases with the applied myosin force  $v$ . Note that the maximum contraction approaches an asymptotic limit as the stiffness asymmetry approaches a ratio of  $\sim 100$ . **C)** Maximum stress achieved during isometric contraction,  $\sigma_m$ , scales approximately with  $\sqrt{\mu_e v}/l_c$ . **D)** Time to reach max stress during isometric contraction scales approximately with  $L\xi/\sqrt{\mu_e v}$ . Scalings for  $\tau_s$ ,  $\sigma_m$  and  $\tau_m$  were determined empirically by trial and error, guided by dimensional analysis.



**S4 Fig.** Filament turnover prevents tearing of active networks. **A)** An active network undergoing large scale deformations due to active filament rearrangements. **B)** The same network as in (A) but with a shorter filament turnover time. **C)** Plots of internal stress vs time for the network in (A). **D)** Plots of internal stress vs time for the network in (B).



**S5 Fig.** Bimodal dependence on turnover time matches bimodal buildup and dissipation of stress in the absence of turnover. **A)** Bimodal buildup of stress in a network with very slow turnover ( $\tau_r = 1000s$ ). **B)** Steady state stress for networks with same parameters as in (Aa), but for a range of filament turnover times.



**S6 Fig.** Dynamics of steady state flow. Plots of stress and strain vs position for networks in which motor activity is limited to the right-half domain and filament turnover time is either **A)**  $\tau_r = 10000$  or **B)**  $\tau_r = 10\text{s}$ . Blue indicates velocity while orange represents total stress, measured as described in the main text.